

1 **Damage in single lap joints of woven fabric reinforced polymeric composites subjected to**
2 **transverse impact loading**

3 R. S. Choudhry^{a,b}, Syed F. Hassan^a, S. Li^c and R. Day^d,

4 ^a College of E&ME Campus, National University of Sciences and Technology (NUST), Islamabad

5 ^b Faculty of Engineering and Physical Sciences, The University of Manchester, Manchester, M13 9PL

6 ^c Faculty of Engineering, University of Nottingham, Nottingham NG7 2RD

7 ^d Glyndŵr University, Mold Road, Wrexham, Wales, LL11 2A

8 **Abstract**

9 Single lap joints of woven glass fabric reinforced phenolic composites, having four different overlap
10 widths, were impacted transversely using a hemispherical impactor with different velocities in the low
11 velocity impact range. The resulting damage was observed at various length scales (from micro to macro)
12 using transmission photography, ultrasonic c-scan and x-ray micro tomography (XMT), in support of
13 each other. These experimental observations were used for classification of damage in terms of damage
14 scale, location (i.e. ply, interfaces between plies or bond failure between the two adherends) and
15 mechanisms, with changing overlap width and impact velocity. In addition, finite element analysis was
16 used to simulate delamination and disbond failure. These simulations were used to further explain the
17 observed dependence of damage on overlap width and impact velocity. The results from these
18 experiments and simulations lead to the proposal of a concept of lower and upper characteristic overlap
19 width. These bounds relate the dominant damage pattern (i.e. scale, location and mechanism) with
20 overlap width of the joint for a given impact velocity range.

21 **Keywords:**

22 Composite Joints; Impact Damage; Disbond; Delamination Modelling; X-ray Micro Tomography

23 **1. Introduction**

24 Joints formed through adhesive bonding or co-curing of composite laminates are often used to form part
25 assemblies for various applications. An important aspect to consider when designing joints having

This is an author's version of post print (final draft after referring) of the journal article in International Journal of Impact Engineering, Volume 80, June 2015, Pages 76-93, <https://doi.org/10.1016/j.ijimpeng.2015.02.003>

26 composite adherends is that the joint or bond interface can have material properties similar to the
27 interfacial material properties of the adherends. This is particularly true for co-cured joints because in this
28 case the polymer matrix within adherends also acts as the adhesive for the joint. Owing to their similar
29 interfacial and joint properties, the failure for such assemblies, when subjected to a multi-axial stress state,
30 is not necessarily more likely to initiate from joint interface (i.e. joint failure). In fact, in some cases the
31 adherends may fail before the joint or the adherends and the joint may fail together. It is for this reason
32 that when discussing failure of such joints due to multi-axial stress state, multiple damage mechanisms,
33 which may occur within plies (fibre and matrix damage), at interfaces between plies (delamination) and at
34 the joint interface (joint failure) also need to be considered.

35 In recent years many authors have analyzed composite bonded joints from various perspectives. For
36 instance, Herszberg et al. [1, 2] undertook FE analysis and proposed a structural health monitoring system
37 for composite ship joints (T – joints) and other marine structures. Their FE analysis was limited to pre-
38 failure linear elastic stress analysis with a view to understand the stress distribution. Li et al. [3-5] used
39 mode I and mixed mode “cohesive zone” models to study the failure of adhesive joints of composites.
40 They used their model to predict joint failure due to lap-shear for a single lap joint. In addition they also
41 simulated the end notch flexure (ENF) test to study the effect of change in mode I failure toughness on
42 failure mechanism. They observed that depending on the mode-I toughness of the joint, the specimen may
43 or may not fail due to interfacial failure. In particular for a relatively strong interface, i.e. with higher
44 mode-I toughness, the composite may fail before the bond failure.

45 Failure of hybrid adhesive/mechanical joints of composites was modelled using a very unconventional
46 approach of Bond-Graphs by Gómez et al. [6]. This technique could only be used to access fail/safe status
47 of the joint and was not used for progressive damage modelling. It also excluded any possibility of
48 modelling failure in composite adherends and only focused on joint failure.

49 In addition to studying the joint failure in standard configurations for quasi-static cases, researchers have
50 also investigated fatigue failure for composite joints. For instance, Ashcroft et al. [7] used electronic

This is an author's version of post print (final draft after referring) of the journal article in International Journal of Impact Engineering, Volume 80, June 2015, Pages 76-93, <https://doi.org/10.1016/j.ijimpeng.2015.02.003>
51 speckle pattern shearing interferometry (ESPSI) and x-radiography to experimentally observe tensile
52 fatigue damage in an adhesively bonded layer. On the other hand, Wahab et al. [8] developed an FE
53 model to predict fatigue life of adhesively bonded multidirectional composites. The model only
54 considered adhesive failure as the dominant damage mechanism. Fatigue life of composite joints was also
55 investigated experimentally by Potter et al. [9]. They studied the effect of fatigue loading using various
56 paste adhesives with unidirectional carbon/epoxy adherends in a double lap joint configuration.

57 There is little work specifically on transverse impact damage of single lap joints of woven composites.
58 There is however, a huge volume of literature available on low velocity impact of laminated composites,
59 which has been an active area of research for over three decades. Since in this study co-cured joints are
60 considered, a number of lessons can be learnt regarding experimental damage characterization and
61 numerical modelling of damage in these joints by consulting this literature. In this regard, the reviews of
62 Richardson et al. [10] and that of Hogg et al. [11] are very thorough and effectively summarise the
63 experimental and numerical work before the start of twenty first century. Hogg et al. [11] in particular
64 also discussed in his review the effect of reinforcement architecture on damage tolerance.

65 Transverse impact produces deformations in localized region around the impact zone (indentation) which
66 may be elastic, plastic or may induce different form of local damage [11-13]. This indentation may
67 subsequently lead to global flexural bending of the structure, penetration/perforation of the specimen or it
68 may lead to a mix of both depending on impact velocity and relative masses of the projectile and the plate.
69 For low velocity impact event, flexural response of the specimen is considered more important and
70 Davies [14, 15] defined it as an impact event in which the through thickness stress wave did not play a
71 role in stress distribution. It was shown by Olsson [16] that the ratio M/M_p (i.e. the ratio of mass of
72 projectile to mass of plate being impacted) can also be used to characterize the type of response of
73 composite square plates. He found that when this value is between '0.2' and '2', the response of plate is a
74 result of interaction between the flexural wave and its boundary conditions. If this value is higher than '2',
75 then a quasi-static response is expected while for values less than '0.2', the response is dominated by the
76 flexural wave (without effect of reflection from boundaries). Thus for identical impact energies, the

77 relative contribution of impactor mass and velocity lead to different damage mechanisms as these
78 possibly excited different frequency modes [17].

79 Most of the studies cited above report damage area measurements using techniques such as 2D X-ray,
80 ultrasonic C-Scan or Microscopy of selected specimens. More recently Richardson [18] experimentally
81 studied low velocity impact induced non-penetration damage in pultruded glass fibre reinforced polyester
82 (GRP) laminates using electron speckle pattern interferometry for live observation of damage. This is an
83 excellent technique, however the main limitation is that it is a 2D technique and information about the
84 exact depth and mechanism of damage is difficult to deduce from this technique alone. In recent years,
85 the use of techniques such as stereoscopic X-radiography and X-ray micro-tomography (XMT) in support
86 of other 2D techniques has gained prominence. As evidenced by [17, 19-22], XMT can provide more
87 information about the damage in 3D and can be used for getting detailed information about damage
88 mechanisms. It has a limitation however, that it is difficult to use it for live capturing of fast occurring
89 events such as impact. Moreover, minute damage in carbon fibres is hard to pick up without the use of a
90 die-penetrant due to low absorption of x-rays in carbon. Stereoscopic X-radiography offers an alternative
91 to XMT for damage characterisation and recently Aymerich et al. [23] have demonstrated that this can be
92 used very effectively to map interfacial impact damage area for each interface within a composite.

93 A number of methods exist for modelling the impact response of composite plates. Abrate [24] has
94 extensively discussed the analytical approaches for studying the impact dynamics for composites and
95 presents several models that can be used to estimate the peak forces and energy absorbed without detailed
96 damage modelling. Most of these models however cannot account for the different boundary conditions
97 and changes in specimen geometry and thus these cannot be directly used for current study where
98 specimen geometry (i.e. in terms of the change in overlap area) and its effect on ensuing damage is under
99 investigation. Different approaches to modelling of damage in composites can be found in literature such
100 as continuum damage modelling (CDM) [25-32], micro-mechanics of damage (MMD) [29, 33], linear
101 elastic fracture mechanics [34-36] cohesive zone models (CZM) [37-39] and synergistic methods [29].
102 The most well-established of these methods for impact damage modelling are the Continuum damage

103 modelling (CDM) based approaches [40, 41] and their recent extensions in the form of cohesive zone
104 models (CZM) that combines the elements of CDM and fracture mechanics [20, 23, 31, 32, 42, 43]. In
105 CDM approaches, onset of failure is usually predicted using a ply level failure criterion [44-47] and the
106 effect of damage growth is reflected through degradation of ply level properties of the material using
107 empirical hardening/softening equations set up in terms of additional material parameters. These
108 additional parameters are adjusted to the model through experimental measurement of loss of stiffness
109 because from the view point of thermodynamics the damage variables are the internal state variables and
110 thus are not measurable directly [29]. Whether the loss of stiffness is sensitive enough or not, to a
111 particular damage mechanism, is arguable [30]. CDM with smeared crack approach [48] has been used
112 more commonly for modelling ply failure mechanisms such as intra-ply matrix cracks (in-plane and
113 transverse) and fibre failure [41], whereas CZM have been used primarily for modelling of delamination
114 failure [29, 39]. CZM models use strength or strain based criterion to either model failure initiation in the
115 same way as traditional CDM or alternately in terms of traction and separation law, and after that, damage
116 propagation is governed by the mode mix of failure and corresponding critical energy release rate ERR
117 [45, 49]. In recent years CZM models have also been used to model intra-ply failure mechanisms in
118 addition to delamination modelling [20, 43]. The main limitation of such models is that the preferred
119 crack paths need to be defined at prior, the computational cost is high and the appropriate calculation of
120 the nine material parameters for each mode of failure being represented by these models is a challenge.
121 CDM models and CZM models have also been used effectively in support of each other [23, 39, 50, 51].
122 In these models the intra-ply failure mechanisms are dealt with using pure CDM approach and
123 delamination is modelled using CZM. Although authors have reported an excellent agreement with
124 experiments in these cases, the general applicability of this approach has the limitation that a significantly
125 high computational cost is required and mesh dependency cannot be completely eliminated. More over
126 the fundamental problems with CDM such as the disagreement about the failure initiation criteria for
127 composites and assumptions about the stiffness degradation schemes remain unresolved. In addition to
128 these other types of synergistic models which combine the elements of other modelling strategies such as

129 CDM and MMD [29] have also been used for modelling damage in composites, however their application
130 to modelling impact damage in composites is yet to be demonstrated to the best of author's knowledge.

131 Unlike the general impact problem for composite plates, the specific question of transverse impact
132 damage in single lap joints of woven composites has been addressed by relatively few researchers. The
133 most notable in these is the work of Kim [52] who specifically looked at damage formation mechanisms
134 in single lap joints having woven glass-epoxy adherends under transverse impact loading. The major
135 limitations of his work were that the experimental portion of his work relied only on ultrasonic C-Scan
136 (2D) and the finite element model was limited to pre-failure analysis. Another directly relevant work was
137 carried out by Bhamare [53]. In this study, the author studied single-lap joints of quasi isotropic and
138 cross-ply laminates under transverse impact. The damage mechanism observation was limited to visual
139 analysis and the model was based on shell element representation of laminates. Delamination failure
140 within adherends was not modelled. The adhesive layer was not modelled physically; instead a tie
141 constraint was used to model the bond. Tie-break failure was then used to model bond failure. Ply failure
142 in this study was modelled using Tsai-Wu criteria for plane stress. As opposed to Bhamare's work [53] a
143 unique aspect of Kim's [52] numerical work was the analysis of both, bond failure and the adherend
144 failure. The study did not simulate progressive failure however, and only delamination initiation was
145 modelled using an empirical quadratic failure criteria. The experimental evidence in that study was
146 limited to two dimensional ultrasonic C-Scans of the samples and thus his work did not provide sufficient
147 experimental data related to through thickness distribution of damage. Other recent studies of adhesively
148 bonded lap joints include work by Quaresimin and Ricotta [54, 55] Odi and Friend [56] and Kim [57].

149 Based on literature discussed above, it can be asserted that the damage mechanisms and the interaction
150 between them for lap joints of composites depends on multiple factors such as joint geometry (e.g. area of
151 overlap region and its thickness), material properties of the laminate and the adhesive, impact velocity,
152 impact energy, location of impact relative to joint geometry and boundary constraints. The review given
153 above is representative of the various approaches that have been followed for analysing damage in
154 bonded composites in recent years. It highlights that firstly only a few authors have specifically looked at

This is an author's version of post print (final draft after referring) of the journal article in International Journal of Impact Engineering, Volume 80, June 2015, Pages 76-93, <https://doi.org/10.1016/j.ijimpeng.2015.02.003>
155 transverse impact induced damage in composite lap joints. Thus for such cases, the change in damage
156 mechanisms with changing impact velocity and joint geometry is not well understood. Secondly, it also
157 highlights that previous researchers have mainly focused on 2D techniques such as C-Scan for damage
158 characterization and damage area measurements. Thirdly, the FE models for most of the previous work on
159 the topic is not sufficiently detailed and the reason for this simplification can often be attributed to the
160 fact that modelling of impact induced damage in composites is a contentious subject area and unlike
161 metals, there is no fundamental agreement on the choice of modelling methodology and failure criterion
162 for composites [10, 11, 58-60]. The disagreement is at various levels, from fundamental understanding of
163 damage mechanisms to choice of modelling methodologies. The issue becomes more complicated with
164 the presence of a joint, since in this case bond failure and its interaction with the composite failure also
165 needs to be considered.

166 **It is understood that the damage mechanisms may also be affected by multiple factors such as impactor**
167 **shape, impactor material, lap joint thickness, type of adhesive and boundary conditions to name a few.**

168 **Discussion of all contributing factors is not possible in a single paper, however. Thus** for single lap joints
169 of composites, impacted transversely by a hemispherical tip impactor; the study aims at clearly explaining
170 the dependence of damage mechanisms and its extent on two of the main contributing parameters, which
171 are impact velocity and overlap width. Experimental methods and FE simulations were both employed to
172 achieve this aim. Experimental methods included transmission photography, ultrasonic c-scan and x-ray
173 micro tomography (XMT). This allowed for observing damage in both 2D and 3D, enabling authors to
174 explain damage mechanism observations in terms of ply, interface and bond failure; taking stock of both
175 macro and micro failure mechanisms. The experiments were supplemented by finite element analysis
176 which was used to simulate impact damage at bond interface and within adherends. Progressive failure
177 through delamination propagation within adherends and the bond layer was modelled using cohesive zone
178 approach [40, 45, 49, 61], while ply failure, i.e. other matrix and fibre failure mechanisms were only
179 evaluated to the point of failure initiation based on different ply failure criteria. The numerical predictions
180 were useful in explaining the experimental observations of damage.

181 **2. The Methodology**

182 Experimental and numerical investigations were carried out as detailed below.

183 **2.1 Details of Experiments**

184 The experimental work was carried out to physically observe transverse impact induced damage in single
185 lap, co-cured joints of woven glass/phenolic composite with a view to characterize the resulting damage.
186 Experiments were carried out in the low velocity regime using a hemispherical impactor, which was
187 much heavier than the lap joint and therefore the results relate with frequently encountered in-service
188 impact scenarios such as tool drop. The choice of velocities investigated was mainly driven by the
189 consideration that while remaining in the low velocity regime a wide range of damage should be
190 observable (i.e. ranging from barely visible impact damage (BVID) to visible impact damage (VID)). The
191 lap joint test specimens were made from Primco-SL246/40, which is a glass fibre/phenolic pre-preg. The
192 pre-preg is based on an 8 harness satin weave fabric impregnated with phenolic resin mix (proprietary
193 modified phenolic resin). The specimens were made using hand lay-up and vacuum bagging using a
194 single side tool. The curing was carried out using Quickstep™ plant at Northwest Composites Centre
195 (NWCC), The University of Manchester (The Quickstep™ process has been described in [62]). **Control**
196 **over thickness variation was ensured by application of vacuum pressure and by the presence of metal**
197 **support strips that were placed above and below each adherend in the non-overlap region. The average**
198 **thickness of the samples in overlap region was 2.4 mm with a standard deviation of 0.09.** The average
199 volume fraction calculated using the Burn-off method (ASTM D3171) was 40.1% and void content was
200 4.5%. Each adherend of the lap-joint was made from four layers of the pre-preg. Thus the overlap region
201 consisted of 8 layers in each case. The joints were co-cured and the resin in the adherends acted as the
202 adhesive; no special surface treatment was required. The layup for each adherend was done in a way that
203 the plies were stacked in the warp direction back to back like flipped pairs. This would result in the layup
204 in each adherend to be semi-symmetric, i.e. $[0/0_f]_2$, where the subscript 'f' refers to the flipping of the
205 alternating lamina and the 0 direction is taken to be along the warp direction. The flipping stacking
206 sequence has been described in more detail in [63].

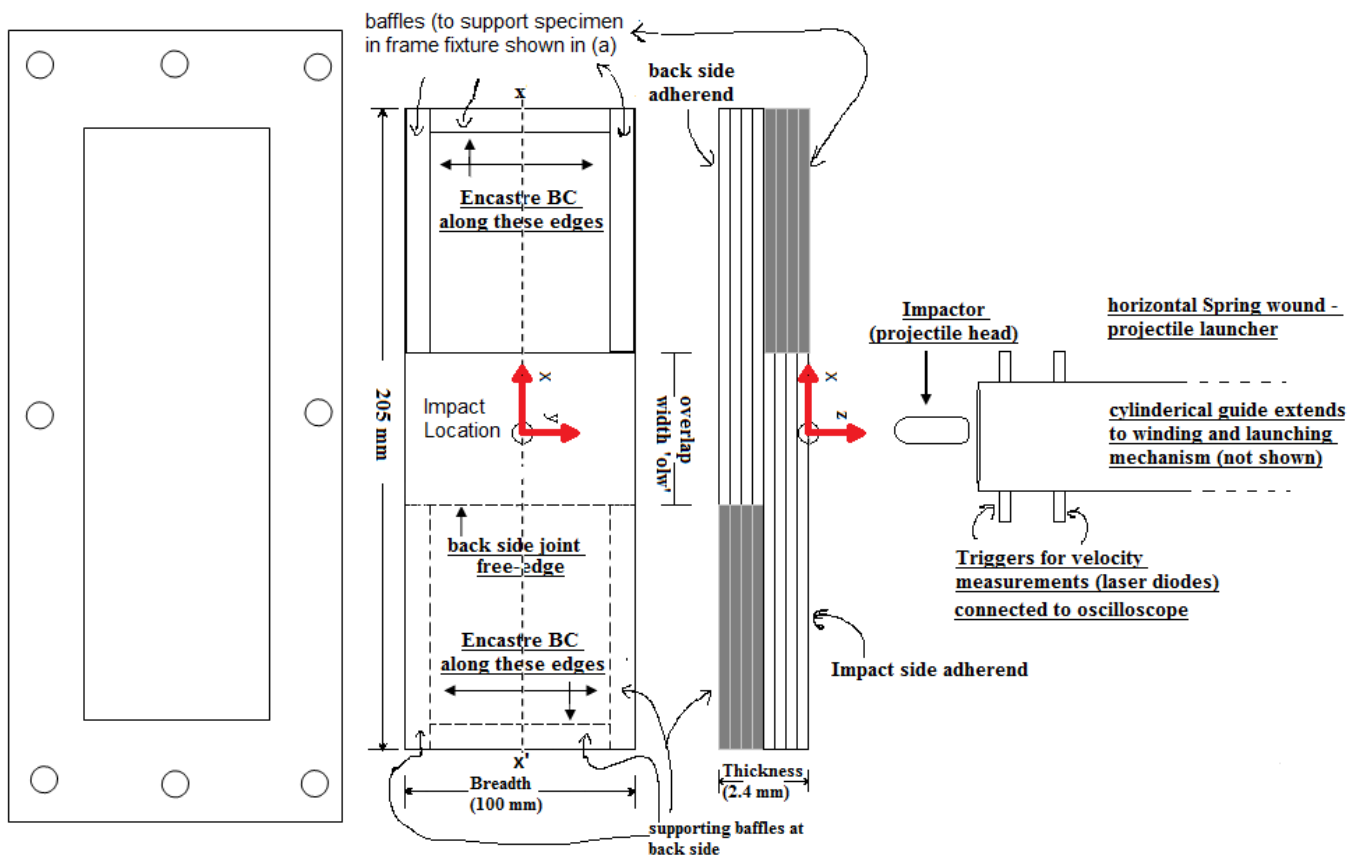
This is an author's version of post print (final draft after referring) of the journal article in International Journal of Impact Engineering, Volume 80, June 2015, Pages 76-93, <https://doi.org/10.1016/j.ijimpeng.2015.02.003>

207 Four different overlap widths (olw) i.e. 21, 25, 36 and 46 mm were tested for a velocity range of 4.0 ms⁻¹
208 to 9.6 ms⁻¹ (which corresponds to the energy range of 1.6 J to 8.0 J) in a horizontal spring loaded impact
209 gun using a hemispherical impactor with tip radius of 7.5 mm and total mass of 201.4 grams. The
210 corresponding ratio of mass of projectile to mass of lap joint for the 21, 25, 36 and 46 mm overlap width
211 joints was 4.4, 4.2, 3.8 and 3.4 respectively. The impactor was not instrumented and through this
212 apparatus it was only possible to measure the velocity before impact (based on a laser diode trigger
213 connected to an oscilloscope), which was then used to calculate the impact energy. No direct impact force
214 or specimen deflection measurements were possible using this apparatus, however peak pressure
215 generated on the test specimen at the point of impact was measured using a pressure sensitive thin film
216 placed under the impact location. The working principle of the film is explained in [64] and the
217 calibration and data reduction has been discussed in [65].

218 A schematic view of the impact test setup is shown in figure 1. The specimens were mounted in the
219 impact rig using a window frame type fixture that consisted of two steel frames between which the
220 specimen is placed (see figure 1). After placing the specimen in the fixture, baffles (cut from the same
221 material as the adherends and having thickness equal to each adherend) were placed around the periphery
222 so that the lap joint was uniformly constrained in the window frame (see figure 1(b) and (c)). Once the
223 specimen and baffles were placed in the fixture, the bolts around the frame (not shown in figure) were
224 fully tightened giving a fully clamped boundary condition (i.e. all translational and rotational DOF = 0) at
225 edges while allowing for bending of the lap joint during test. The free breadth, i.e. taking in account the
226 constrained portion of the lap joint, was around 96 mm. In the above velocity range, tests were carried out
227 at five different velocities with at least three repeats for four of these velocities and a single test for each
228 specimen at lowest velocity.

229 Each sample was examined for damage using ultrasonic C-Scan and through transmission photographs
230 (imaging) after the impact tests. The system used for performing C-Scan was a 2-axis computer
231 controlled water jet inspection system from 'Midas NDT' (used in through transmission mode with
232 unfocussed, 10 MHz probes) and imaging was done using Nikon D200 Camera (The backside
233 illumination was achieved by placing the sample flat on the glass top of a standard slide projector whose

234 diffuser had been removed to allow for maximum light). The damaged area as percentage of overlap area
 235 was calculated using a comparison of the pre-impact and post impact scans and images. Ultrasonic C-
 236 Scan and imaging offered comparable results of damage in 2D owing to the transparent nature of glass
 237 fibres and the fact that the thickness was also less (2.4 mm). These results albeit useful were not sufficient
 238 to describe the damage mechanisms in 3D and at micro level. Thus, a number of samples were chosen for
 239 damage mechanism observation using X-ray micro-tomography (XMT).



a) Steel frame (top view) in which the specimen (b) was clamped before being impacted

b) Specimen (top view)

c) Specimen (side view)

d) Impact loading gun (side view)

240

241 **Figure 1:** Schematic representation (not to scale) of impact testing setup and specimens.

242 XMT is one of the computed tomography (CT) techniques and refers to reconstructing a volume from its
 243 cross sectional projections. The cross sectional projections are obtained from x-ray transmission data.
 244 Since different materials absorb x-rays to different extent the internal micro-structure of an object can be
 245 revealed using the contrast difference. The XMT system used for this study was HMXST 225 supplied by
 246 X-Tek systems Ltd. Details of the equipment were discussed in [65] and details of technique can be read
 247 from [66]. In case of glass phenolic composites, XMT works particularly well because the level of

This is an author's version of post print (final draft after referring) of the journal article in International Journal of Impact Engineering, Volume 80, June 2015, Pages 76-93, <https://doi.org/10.1016/j.ijimpeng.2015.02.003>

248 attenuation offered by both the constituents is significantly different. This technique allowed for

249 observing damage at any location within the specimen. Virtual cross sectional images and 3D surface

250 views were generated at any required depth and angle without any need for physical cutting. Multi-planar,

251 cross-sectional views were used to investigate the connectivity of damage in three dimensions. As an

252 example of the XMT carried out in this study, figure 2a shows three orthogonal slices through the overlap

253 region of a 21 mm overlap width joint impacted at 6.7 ms^{-1} velocity. Figure 2b shows for the same scan, a

254 single oblique slice through the specimen, at a location where both delaminations can be seen

255 simultaneously. XMT scans results in hundreds of such slices through the specimen (depending on

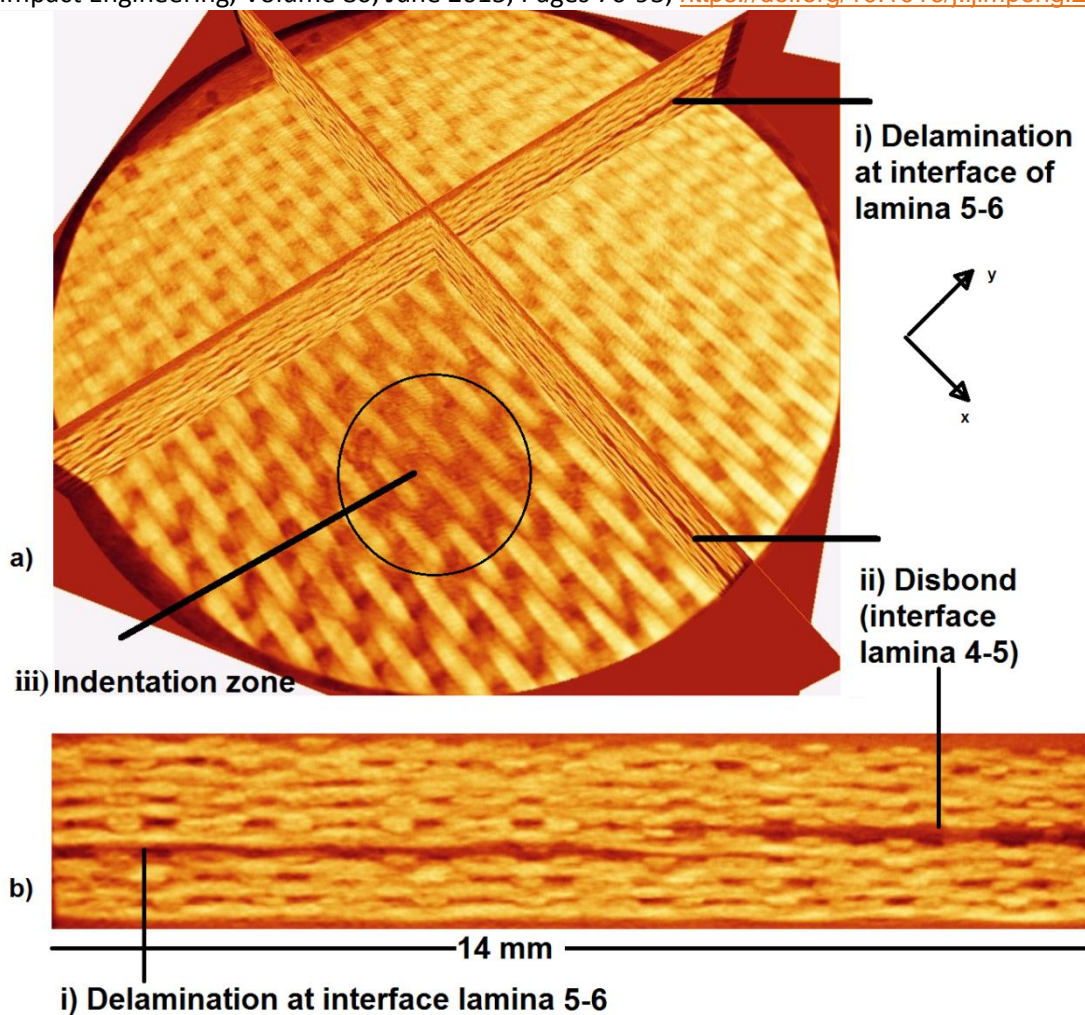
256 resolution and area scanned). It can be seen from this example that this technique enabled the authors to

257 determine the location, extent and connectivity of damage within a sample. The scan shown in figure 2

258 was performed at a resolution of $20.3 \mu\text{m}$ voxel size. Using scans at higher resolution (up to $10 \mu\text{m}$) even

259 more detailed damage features were studied. For each specimen XMT was done at various resolutions,

260 thus revealing damage features ranging from millimetres to micro metres.



261

262 **Figure 2:** Sectional views using X-ray micro tomography for identifying the damage mechanisms in 3D

263 (a) Three orthogonal slices from an XMT scan (resolution 20.3 μm) (b) Oblique section view from the

264 same scan showing delamination and disbond simultaneously.

265 In addition to these tests, microscopy of some selected samples was also carried out to observe the surface

266 at delaminated interface. The remaining samples were tested for residual bond strength. Besides the

267 impact tests, other tests such as the mixed mode bending tests for determining the fracture energies at

268 various mode mixes (from pure mode I to pure mode II), three rail shear test to determine the shear

269 modulus and tensile tests for finding tensile modulus were also performed. These tests were used for

270 specifying the properties in FE model and were performed following applicable standard test methods.

271 The details of these tests can be found in [65].

272 **2.2 Details of Simulations**

273 Explicit time integration was used to carry out a dynamic simulation of the actual impact event using
274 finite element analysis software package ABAQUS/Explicit.

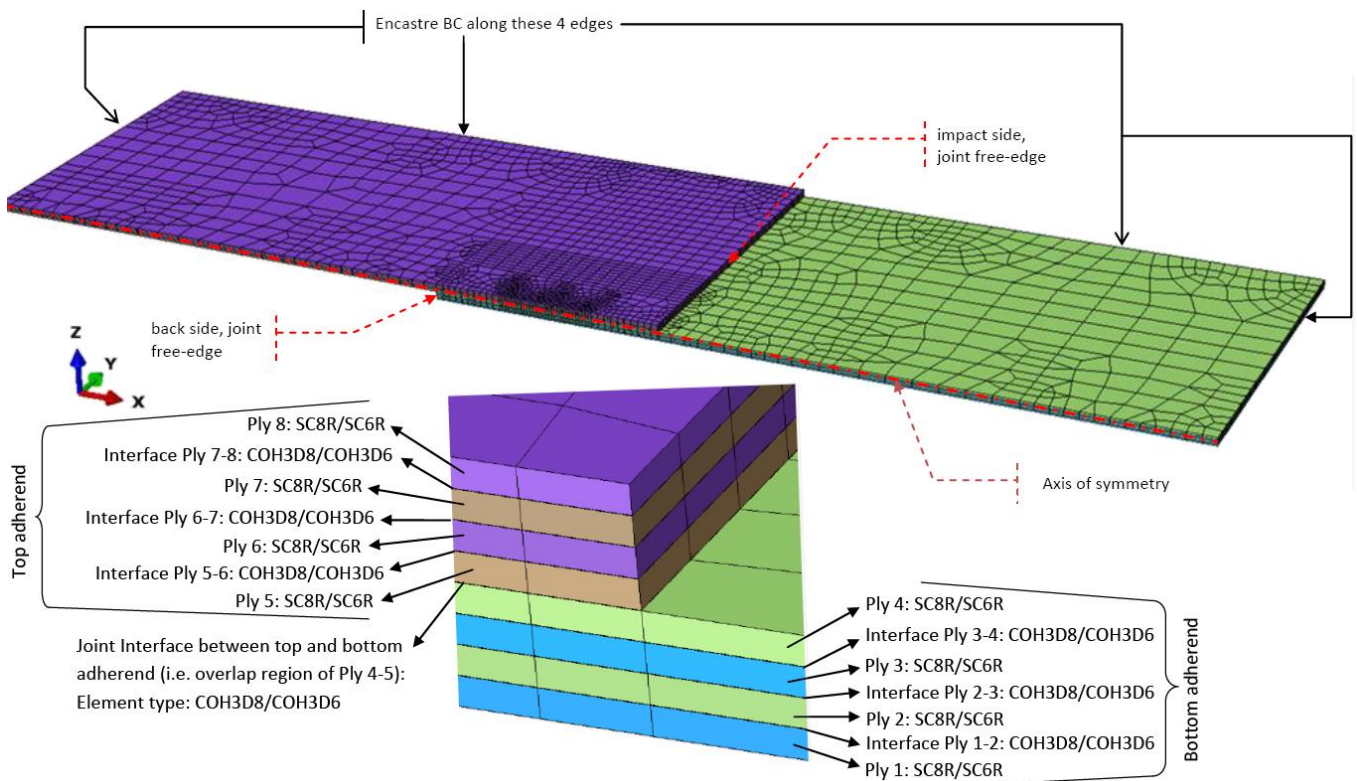
275 **2.2.1 Model Geometry and Boundary Conditions**

276 The model geometry and boundary conditions were specified as shown in figure 3. These boundary
277 conditions closely approximated the boundary conditions described earlier for the actual experimental
278 setup. FE simulations were carried out for all the lap joint geometries and impact velocities used in
279 experiments. The impactor was modelled as an 'analytically rigid' part and velocity was specified as a
280 'pre-defined field variable'. The projectile was constrained to move only along z-axis, thus not allowing
281 for any slip of projectile during impact. The dynamic interaction between the projectile and the lap joint
282 was modelled as frictionless 'hard contact' [67] in Abaqus/Explicit.

283 **2.2.2 Mesh details**

284 Each ply within the adherends and each interface between adjacent plies, was meshed using a separate
285 layer of elements. Similarly, the bond interface (joint) between the two adherends was also meshed using
286 separate layer of elements. This has been shown in zoomed view of mesh in figure 3. Thus each ply was
287 meshed using a single layer through the thickness of reduced integration continuum shell elements (i.e. 8
288 node, reduced integration, hexahedron (SC8R) and 6 node reduced integration wedge (SC6R) [68]). Each
289 of the layers (i.e. each ply) was connected to other through interface layer that was meshed using 8 and 6
290 node, three dimensional, cohesive zone elements (COH3D8 and COH3D6) [69]. The joint interface (bond
291 layer) in the overlap region was also modelled using similar cohesive elements. The cohesive layer was
292 generated using an offset mesh, meaning that the in-plane density of the mesh for the interfaces and the
293 plies was the same; in fact, they had shared nodes at mating surfaces. **Each continuum shell element had
294 one element integration point and three section integration points (numerical integration of shell section
295 using Simpsons rule), while each cohesive element had one element integration point. Thus in total the
296 mesh had fifteen integration points through the thickness for the lap joint in the overlap region for the
297 converged mesh (i.e. one for each ply and one for each cohesive zone). For the continuum shell elements,
298 the outputs were requested at three section integration points for each ply (i.e. the top, mid and bottom**

299 portion of each element) and hence, the outputs were available at thirty one points through the thickness.
300 Through thickness mesh density, similar to the one used in this study, has been found adequate to capture
301 the bending and indentation response by other authors [20, 23]. In order to ascertain this however,
302 comparable simulations having two stacked 3D continuum solid elements (C3D8R) for each lamina were
303 also run. These models had twenty three integration points through the thickness as opposed to the fifteen
304 discussed earlier. The results however, did not show any appreciable change in the measured damage area
305 or peak contact force history, thus the mesh with one continuum shell elements and one cohesive element
306 per ply was used for the remaining simulations. The choice for using continuum shell elements instead of
307 solid elements was guided by the fact that as opposed to solid elements these did not have any restriction
308 on aspect ratio.



309
310 **Figure 3: Mesh details and boundary conditions (only half lap joint is shown for visualization purposes)**

311 The problem being modelled had three main sources of mesh dependency. The first one was due to
312 modelling of contact between the lamina outer surface and the projectile outer surface. The mesh in this
313 case had to be refined enough in the impact zone to prevent penetration of projectile into the lamina. This
314 was successfully achieved and validated. The second source of mesh dependency was due to the reason

This is an author's version of post print (final draft after referring) of the journal article in International Journal of Impact Engineering, Volume 80, June 2015, Pages 76-93, <https://doi.org/10.1016/j.ijimpeng.2015.02.003>

315 that contact between each lamina was handled by cohesive zone elements rather than by explicitly
316 defining contact surfaces. The cohesive elements even after failure resist penetration under normal
317 compression and small amount of shear loading. When the shear loading is large (relative to element
318 dimensions), the elements may distort and allow interpenetration of plies [65, 70]. This was prevented by
319 having a sufficiently refined mesh in the impact zone and around it. The third source of mesh dependency
320 was related to the energy dissipation during the strain softening phase of modelling progressive damage in
321 continuum elements. This was resolved by using a characteristic length in the formulation of cohesive
322 element [65, 70]. Due to this characteristic length it was possible to define the damage propagation using
323 a stress – displacement relation instead of stress-strain relation. Thus in this case, the energy dissipated
324 during the damage process was specified per unit area rather than per unit volume. This allowed for a
325 direct relationship between this energy and crack propagation displacement in a manner similar to the
326 fracture mechanics approach of using critical energy release rate. Use of similar formulation has also been
327 reported by [20, 23] and was found to greatly reduce the mesh dependency.

328 As indicated earlier, the mesh in XY plane in the overlap region and in particular in the indentation zone
329 (i.e. the region with maximum possibility of damage) was denser than other regions. Such biasing of
330 mesh for explicit analysis has also been reported in [20, 23, 39]. Since, explicit integration scheme was
331 being used therefore it was expected that this biasing may cause some deviation of results as in certain
332 regions stress wave propagation may not be captured adequately. This biasing was inevitable however,
333 due to the limitation of computational resources required for the large number of cases to be run. If the
334 entire mesh was made with a uniform mesh size of the smallest element edge length (i.e. 0.375 mm) then
335 the mesh for 21 mm overlap joint (the smallest mesh case) had over a million elements (1,050,112
336 elements: 591,872 SC8R and 458,240 COH3D8) as opposed to around fifty thousand elements (51,328
337 elements: 27,304 SC8R; 784 SC6R; 22588 COH3D8 and 652 COH3D6) required for the biased mesh.

338 The results of the sensitivity analysis showed that even with the use of over a million elements the
339 maximum damage area did not change more than 3% and the differences in peak contact force and
340 displacement were even smaller.

341 Based on this, it can be concluded that the final mesh selected had to be a compromise between the
 342 quality of output and the computation time required for each case. This was considered acceptable
 343 because the variation in experimental damage area measurements (as commonly happens in composites)
 344 was also of a higher degree and because the intent of study was to explain the damage modes rather than
 345 generating design parameters.

346 **2.2.3 Material model and failure criteria for adherends excluding interfaces and joint**

347 The material model for each ply (i.e. each layer of continuum shell elements) was written in FORTRAN
 348 programming language and implemented via the user subroutine interface VUMAT in ABAQUS/Explicit.
 349 This material model was modified from the built in material model type 'lamina', which was a plane stress
 350 transversely isotropic (orthotropic) elastic material model. The modified material model followed the
 351 approach described by Li *et al.*[71] and thus took in account, in-plane shear non-linearity of the
 352 composite, by using a piece-wise bilinear approximation to the non-linear shear stress-strain curve. The
 353 material model can be described by the following set of equations,

$$\begin{aligned}
 354 \quad \tau_{11i} &= \tau_{11i-1} + (Q_{11} * \Delta\varepsilon_{11i} + Q_{12} * \Delta\varepsilon_{22i}) \\
 355 \quad \tau_{22i} &= \tau_{22i-1} + (Q_{21} * \Delta\varepsilon_{11i} + Q_{22} * \Delta\varepsilon_{22i}) \\
 356 \quad \tau_{33i} &= 0 \quad (\text{The actual out of plane stresses are not zero as will be explained subsequently.}) \\
 357 \quad \tau_{12i} &= \tau_{12i-1} + G_{12} \Delta\gamma_{12i} \text{ for } |\tau_{12i}| \leq |\tau_{nl}| \\
 358 \quad \tau_{12i} &= \tau_{12i-1} + G_{12}^{nl} \Delta\gamma_{12i} \text{ for } |\tau_{12i}| > |\tau_{nl}| \\
 359 \quad \Delta\gamma_{12i} &= \gamma_{12i} - \gamma_{12i-1}
 \end{aligned} \tag{1}$$

360 Where, i, represents the ith increment for which computation is being carried out in ABAQUS/Explicit
 361 and '1' axis is taken along the warp direction and '2' axis is taken along the weft (fill) direction.

$$362 \quad Q_{11} = \frac{E_1}{1 - \nu_{12} \cdot \nu_{21}}; Q_{22} = \frac{E_2}{1 - \nu_{12} \cdot \nu_{21}}; Q_{12} = \frac{\nu_{21} \cdot E_1}{1 - \nu_{12} \cdot \nu_{21}}; Q_{21} = Q_{12} \text{ and } \nu_{21} = \frac{E_2}{E_1} \nu_{12}; G_{12} \text{ is the shear}$$

363 modulus in the linear range and G_{12}^{nl} is the linear approximation for the shear modulus in non-linear range
 364 and τ_{nl} is the stress level after which the non-linear shear behaviour was observed in a three-rail shear test
 365 as described in [65]. In the above equation the out of plane stress component (τ_{33}) has been set to zero.

366 This apparent anomaly is because for continuum shell elements like all shell elements the assumed stress
367 state for constitutive relation is plane stress and thus out of plane stress component is reported as zero for
368 these elements in ABAQUS. This however does not mean that the actual out of plane normal and shear
369 components are zero as these are calculated based on the shell section properties as explained in detail in
370 ABAQUS analysis user manual [72] and hence their definition is not repeated here. The input material
371 properties used for defining each lamina for FE analysis are given in table 1. Note that in this table the out
372 of plane section modulus was taken equal to the out of plane modulus of composite laminate while the
373 transverse shell stiffness was specified as a function of ply thickness as recommended in the ABAQUS
374 theory manual [73].

375 The material model used in this study does not take in account the strain rate sensitivity of composite and
376 the adhesive layer. As opposed to CFRP materials, GFRP composites are known to be somewhat rate
377 sensitive [20]. In absence of reliable material data at different strain rates however, the authors were
378 compelled to make a judicious choice between either running the model with assumed data; or not to
379 consider the rate effects at all. In this regard the paper of Heimbs et al. [74] was consulted. He
380 experimentally evaluated the strain rate sensitivity of phenolic woven-glass fibre reinforced composites
381 for the strain rates ranging from 10^{-4}s^{-1} to 50s^{-1} . He found out that there was an 88% increase in peak
382 uniaxial tensile strength value in warp direction, 53% increase in weft direction and around 33% increase
383 in shear strength but there was little change in elastic modulus. Thus the authors concluded that by
384 ignoring the rate effects the model will be conservative and may predict more damage than the
385 experimentally observed damage (which was verified later). Since the intent of modelling in this paper is
386 not to generate design allowable rather it is to help understand the damage process, this simplification was
387 preferred over running the model with assumed material data.

388 It is pertinent to mention that unlike delamination modelling, progressive failure was not modelled for the
389 ply or lamina failure mechanisms. Only failure initiation stresses were evaluated by comparing three
390 failure theories. These were the LARC03 (Langley research centre criteria 03) [45], Tsai-Wu criterion [46]
391 and Max Stress theory [46]. The equations defining the failure indices for all these theories were
392 implemented as part of the user subroutine mentioned earlier. There were a number of reasons for not

This is an author's version of post print (final draft after referring) of the journal article in International Journal of Impact Engineering, Volume 80, June 2015, Pages 76-93, <https://doi.org/10.1016/j.ijimpeng.2015.02.003>

393 modelling the ply failure in this case. Firstly, there is no consensus amongst researchers that which

394 progressive damage modelling methodology should be adopted. Secondly, if the author had opted for

395 continuum damage modelling (CDM) approach there is no consensus on which failure criteria should be

396 used to derive the model required for modelling the ply failure. Thirdly even if a CDM based on LARC03

397 or Hashin damage is adopted [23, 45], even then the experimental effects of damage in woven composite

398 in most cases cannot be adequately captured by these models which are primarily aimed at unidirectional

399 or at best multi-directional laminates. Although there are better approaches in literature for modelling

400 damage in woven composites [75], the material data required for these models was difficult to obtain and

401 this may be taken up as future work in a study that improves the current model. Thus, the consequences of

402 this simplification were weighed against the quality of results obtained. Experimental observations

403 revealed that for the smaller overlap width joints, delamination and disbond were the dominant damage

404 mechanisms. Thus, in these cases it was expected that deviation of simulation results from experimental

405 values will be small. Even for cases of larger overlap width joints, for the velocity range under

406 consideration, complete penetration of projectile or complete splitting of adherends was not observed

407 experimentally, therefore, the results without modelling delamination failure were considered acceptable.

408 The consequences of this assumption have been discussed further in the results section.

409 **Table 1: Material properties for the individual ply used in FE models for Continuum Shell elements**

Density of composite	= 1566.3 kg.m ⁻³
E_1 : Tensile modulus in 1 direction (Warp)	= 24.2 GPa
E_2 : Tensile modulus in 2 direction (Weft)	= 23.1 GPa
ν_{12} : Poisson ratio	= 0.2
G_{12} : (in-plane shear modulus in linear range)	= 3.85 GPa
G_{12}^{nl} : (in-plane shear modulus non-linear range)	= 1.04 GPa
<u>Section properties for out of plane section stresses</u>	
E_3 : Out of plane section modulus	= 7.71 GPa
$K_{11} = K_{22}$: transverse shear stiffness of the shell section in 13 and 23 plane	= 0.482 MPa
<u>Lamina Strength</u>	
X_t : Tensile stress limit in warp direction	= 336.6 MPa
X_c : Compressive stress limit in warp direction	= -298.4 MPa
Y_t : Tensile stress limit in weft direction	= 295.8 MPa
Y_c : Compressive stress limit in weft direction	= -309.4 MPa
S_{12} : Shear strength in the X-Y plane	= 57.2 MPa

410 **2.2.4 Material model for the joint interface and the interfaces within adherends**

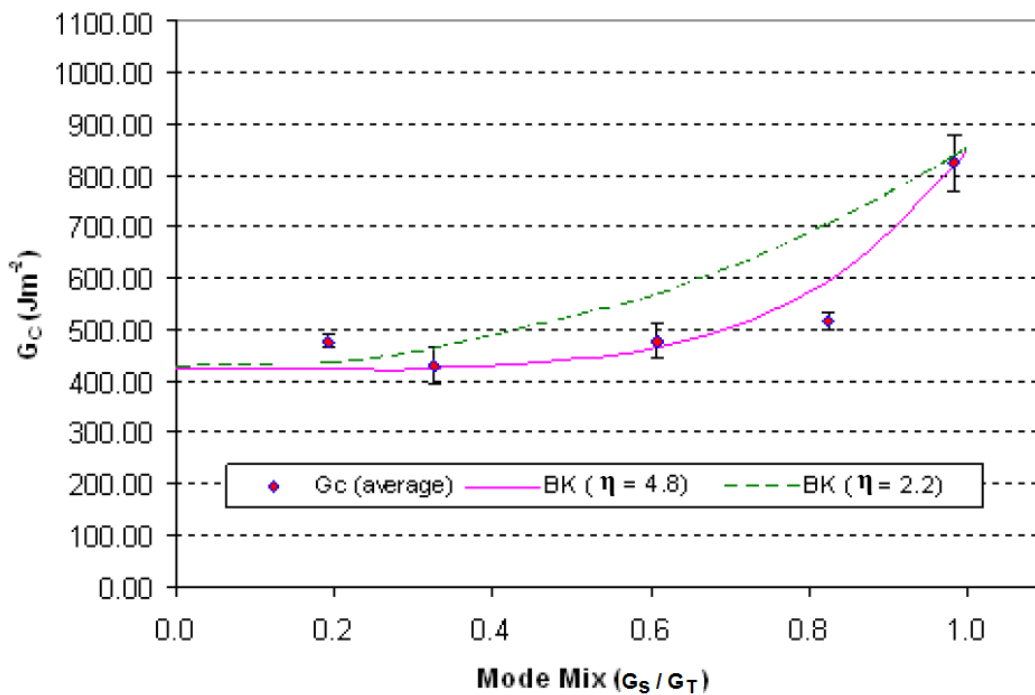
411 The joint interface (bond interface), the interfaces within adherends and their subsequent disbonding and
412 delamination were modelled using cohesive zone elements. The material model used for these elements is
413 based on traction-separation description of the interface [76, 77]. This approach allows for failure
414 initiation prediction using a stress or displacement based failure criterion while the propagation is
415 controlled by comparing the energy release rate (ERR) with the experimentally determined critical energy
416 release rate (G_c) for this material. Since in this problem the mode of failure (i.e. normal, shearing or
417 tearing) was not known at prior, a mixed mode cohesive model as described in [26, 77, 78] was used.
418 The interfacial tractions (τ_i) were defined as $\tau_i = K_i^o \cdot \delta_i$; where $i = I, II, III$ represented the three modes of
419 crack propagation (i.e. normal, shearing or tearing), and δ_i were the corresponding separations between
420 the opposite faces of the cohesive zone elements. The interface behaviour was assumed linear elastic up
421 to crack initiation and damaging elastic thereafter. K_i^o is the penalty stiffness value and following Zhou et.
422 al. [25], it was defined as $K_i^o = K_i \cdot \tau_i^c$ where τ_i^c ($i=I,II,III$) are the interlaminar tensile and shear strengths
423 respectively and the constant K_i can be assigned any value between $1E5 \text{ mm}^{-1}$ to $1E7 \text{ mm}^{-1}$. In this study
424 K_i was fixed at $1E6 \text{ mm}^{-1}$ while the values of τ_i^c (as reported in table 2) were estimated from the tensile
425 lap shear tests performed on single lap joints. Thus based on these values the penalty stiffness was
426 evaluated using the previously defined equation $K_i^o = K_i \cdot \tau_i^c$. It may be pointed out that the choice of this
427 penalty stiffness also satisfies the requirement posed by ABAQUS for stable time increment [79]. The
428 failure index (FI) for damage onset in the interface zone was calculated using quadratic nominal stress
429 criterion defined in ABAQUS [70]. This was preferred over the maximum stress criterion because the
430 polymer matrix due to transverse impact is under considerable multi-axial stress state, and the quadratic
431 criterion is interactive and can thus more effectively take in account the interaction of different stress
432 components.

433 After failure initiation the traction is progressively reduced using a scalar damage parameter. The
434 evolution of this damage parameter (i.e. the damage evolution law), depends on how the ERR, for the
435 damaged element (from FE analysis), relates with the critical energy release rate (G_c) for that mode mix

This is an author's version of post print (final draft after referring) of the journal article in International Journal of Impact Engineering, Volume 80, June 2015, Pages 76-93, <https://doi.org/10.1016/j.ijimpeng.2015.02.003> (based on experiments). The dependence of G_c on mode mix was specified using the Benzeggagh-Kenane (BK) criteria [78]. The BK criteria can be mathematically expressed as,

$$G_c = (G_{IIc} - G_{Ic}) \cdot \left(\frac{G_s}{G_T}\right)^\eta \quad (2)$$

Where, G_{Ic} is the pure mode I critical energy release rate and G_{IIc} is the pure mode II critical energy release rate. $G_s = G_{II}$ is the mode II component of the energy release rate for a mixed-mode situation and $G_T = G_I + G_{II}$ is the sum of mode I and mode II components of energy release rate for a mixed mode problem. $\frac{G_s}{G_T}$ defined the mode mix for which the G_c value had to be approximated and η is a material parameter that gave the best fit to the experimentally determined G_c values measured from standard mode-I and mixed mode bending tests (details of these test can be found in [65]). The results of these tests and BK criteria fit to the test data for two different values η is shown in figure 4. The material data input for the cohesive zone model is given in Table 2. It should be pointed out that since no material data was available for mode III, therefore in keeping with the usual practice G_{IIIc} was assumed to be equal to G_{IIc} , while implementing the model in ABAQUS.



BK criteria fit to the experimental data for $\eta = 2.2$ and 4.8

449 **Figure 4:** Experimentally measured fracture energies for various mixed mode ratios and BK-criteria fit
 450 to the data with two different values of parameter η .

452 **Table 2: Material properties for the cohesive zone elements in FE models**

Density of resin (to be used for cohesive zone)	= 1085.0 kg.m ⁻³
$K_{nn} = K_I^o$: Penalty Stiffness in mode I	= 4440 GPa
$K_{ss} = K_{II}^o$: Penalty Stiffness in mode II	= 2220 GPa
$K_{tt} = K_{III}^o$: Penalty Stiffness in mode III	= 2220 GPa
τ_I^c : Inter-laminar tensile strength	= 44.4 MPa
$\tau_{II}^c = \tau_{III}^c$: Inter-laminar shear strength	= 22.2 MPa
G_{Ic}	= 425 J.m ⁻²
G_{IIc}	= 905 J.m ⁻²
η	= 4.8
Softening	= Exponential

453 3. Discussion of Results

454 Different combinations of multiple damage mechanisms, such as indentation, matrix cracking,
455 delamination, bond failure (disbond), tow splitting, fibre fracture (weave failure) and bulging were
456 observed to varying extents for the lap joints impacted at different velocities. It was also observed that
457 there is a strong dependence of observed damage mechanisms and area of damage on overlap width and
458 impact velocity.

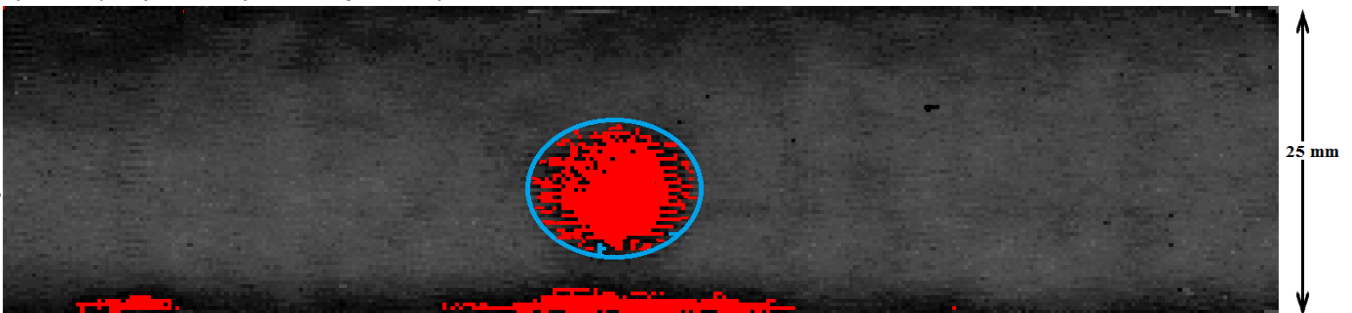
459 3.1 Damage area measurement

460 Damage area was calculated both experimentally using C-Scan and theoretically using FE simulations.
461 Figure 5 shows a representative C-Scan for a test specimen and a corresponding FE simulation result. The
462 red zone in Figure 5(i) indicates damaged area as measured using ultrasonic C-Scan. The value of
463 experimental percentage damage area from C-Scan plotted in figure 6 was calculated by taking average of
464 up to three tests results like the one shown for each impact velocity and overlap width. In figure 5(ii), the
465 plot of damage variable (SDEG) for the cohesive zone elements at the bond interface, (i.e. failure of
466 cohesive zone between lamina 4 and 5) measured from FE simulation, is shown. The red region shows
467 elements which are more than 90% degraded. Such plots were drawn for all interfaces, overlap widths
468 and impact velocities. It was observed that in each case the most severely delaminated interface is the
469 bond interface. Thus based on such plots the damage area measured from FE analysis was calculated for
470 each case. **It may be pointed out that the damage area measurements for C-Scan were taken after the**
471 **completion of test (i.e. once the elastic spring back had taken place) and required physically removing the**
472 **sample from the rig, while for simulation results the area was measured after 1.81ms of the first impact.**
473 **By this stage, although the specimen had not become completely stationary, it had rebounded and the**

474 vibrations were slowly decaying and damage area was not changing appreciably. There can be an
475 argument that the simulation could have been allowed to run longer i.e. until the specimen had completely
476 stopped, but this would have required much longer computational time without any appreciable increase
477 in damage area.

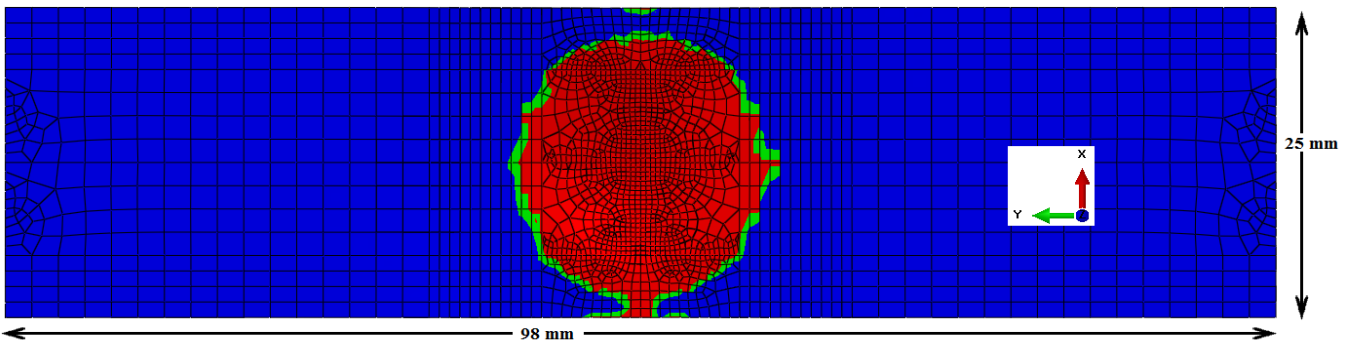
478 Figure 6 compares the damage area values expressed as percentage of overlap area in each case for both
479 experiments and FE simulations. This graph shows that the FE analysis predicts more damage than
480 observed experimentally, however for both, the data trend, i.e. damage area reduces with increasing
481 overlap width, is consistent. Thus in general, the data trend for experiments and simulations agree and the
482 model results can be considered as conservative. The over prediction of model results can be explained
483 with the help of x-ray micro tomographic evidence. XMT shows that there was significant interaction
484 between inter-laminar and laminate failure mechanisms.

i) C-Scan (Sample A18: impact velocity 6.7 ms^{-1})

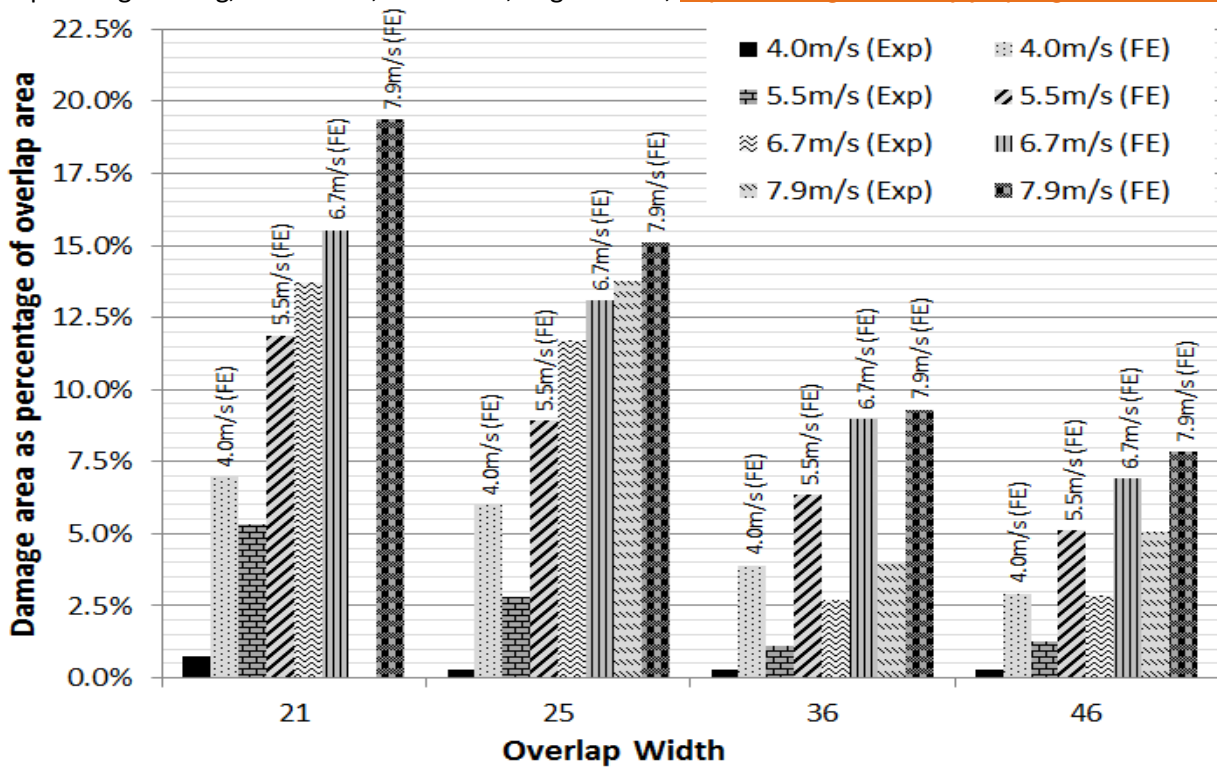


ii) Corresponding FE Results (Plot of damage variable for bond interface)

1.00 SDEG = Damage variable:
0.90 1 shows completely (100%) degraded cohesive element.
0.50
0.00 0 indicates no damage



485
486 ***Figure 5: C-Scan of overlap area of one of the test specimens and a corresponding FE simulation result***
487 ***showing contour plot of damage at bond interface.***



488

489 **Figure 6:** Comparison of FE damage area prediction and average experimental damage area values
 490 from C-Scan expressed as percentage of total area of overlap in each case for the scenarios where impact
 491 velocity was 4.0 ms^{-1} , 5.5 ms^{-1} , 6.7 ms^{-1} and 7.9 ms^{-1} .

492 It will be explained in more detail later that for the higher velocity cases of wider joints significant macro
 493 laminate failure mechanisms were observed. Significant energy may be dissipated in these failure
 494 mechanisms and in addition to this the failed or collapsed weave sometimes created physical barriers to
 495 delamination crack opening. The consequence of this damage mechanism interaction is that regardless of
 496 the severity of damage in the damage zone the actual extent of delamination area (which is what C-Scan
 497 is measuring) will be less for such cases. On one hand, this highlights the limitation of using C-Scan and
 498 other similar 2D techniques alone because they only measure the 2D projection of damage area which
 499 does not necessarily always reflect the severity of damage. On the other hand, this also points out the
 500 limitation of the model that unless the model completely captures the damage mode interaction it will fail
 501 to capture the true extent of delamination. A model which only models delamination failure may predict a
 502 larger damage area than the one actually observed in experiments because firstly there is no possibility of
 503 modelling the physical barrier that the collapsed or pushed-out weaves from adjoining plies create for

504 propagation of delamination. Secondly, in such a model the kinetic energy of the projectile must either be
505 converted into elastic strain energy of the laminate or be used for advancing the delamination crack front.
506 This will result in a larger delamination area as compared to a model, in which part of the kinetic energy
507 of the projectile had also been utilized for advancing the damage in the adjoining ply itself. Such
508 limitation of a model that only accounts for delamination has also been recently reported by Aymerich et
509 al. [23]. Despite the limitations, the FE simulations gave useful insight into the damage propagation
510 mechanism; and when reviewed together with the experimental observations these were also useful for
511 explaining the evolution of various damage mechanisms.

512 **3.2 Characterization of damage mechanisms**

513 The presence of multiple damage mechanisms made it difficult to identify a pattern or trend in the
514 evolution of damage with change in overlap width and impact velocity. The pattern however became
515 more evident once damage mechanisms were categorized under the two well-known broad classes. That
516 is, the **laminar failure mechanisms**, which included both fibre and matrix failure mechanisms at micro
517 and macro length scales (such as indentation, matrix cracking, fibre fracture, weave failure etc.), and
518 **inter-laminar failure mechanism** which included delamination within adherends and disbond (which is
519 defined as the delamination that occurred specifically at joint interface between the two adherends in
520 overlap region). The damage mechanism observations for all sets of experiments have been summarised
521 in table 3 and will be discussed subsequently.

522 **3.2.1 Laminar failure mechanisms**

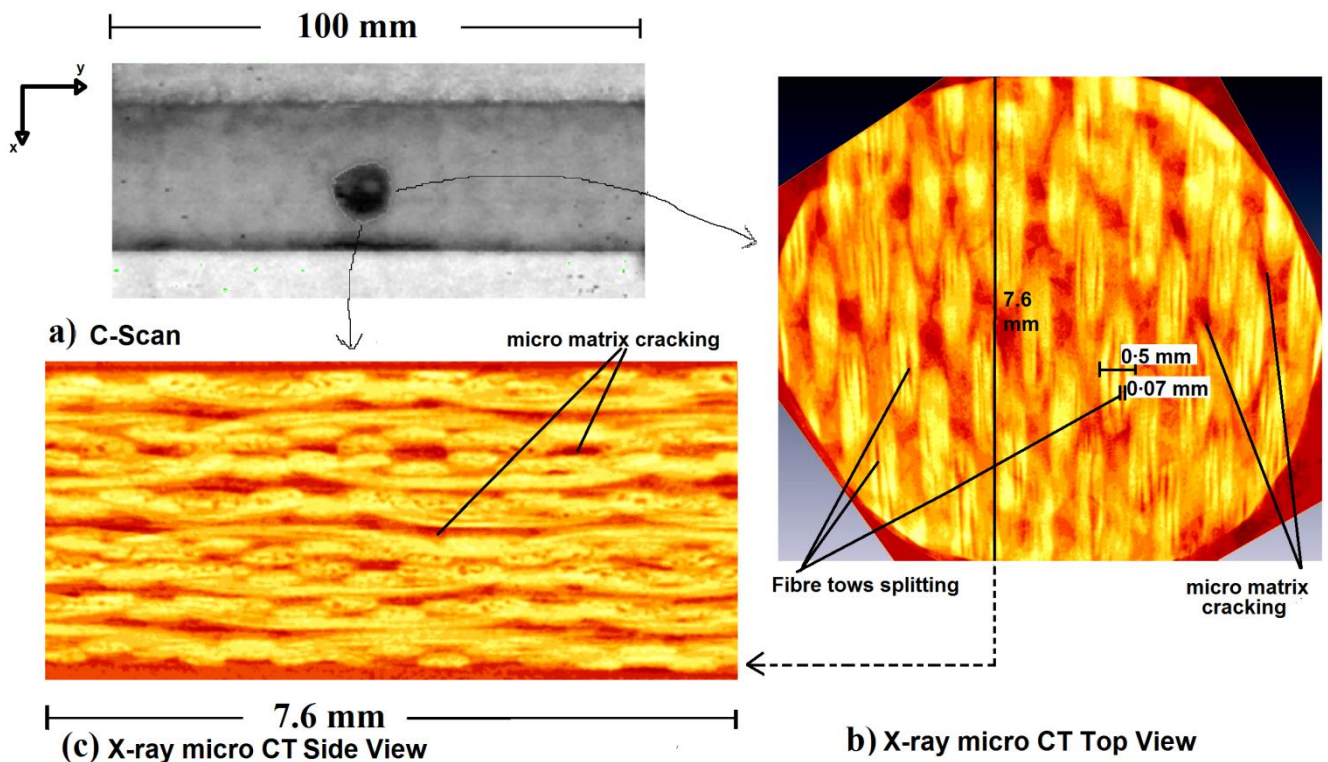
523 The laminar failure mechanisms can be further classified in terms of length scale at which these occur i.e.
524 **Micro** or **Macro** failure mechanisms.

525 **(a) Micro Laminar failure mechanisms**

526 Once the hemispherical projectile impacted the top surface of the adherend; before the lap joint could
527 bend significantly as a whole structure; local deformation under the nose of impactor took place. The
528 severity of local indentation for a composite panel was previously shown to be linked with mass of
529 projectile [17]. In this study the mass of impactor was kept constant throughout and only velocity was

530 varied. The results showed that for single lap joint having composite adherends the overlap width played
531 a significant role in determining whether the overall flexural response or the local indentation dominated.
532 As summarized in Table 3, for cases where either the impact velocity was low (6.7 ms^{-1} or less) or where
533 the overlap width was small (the 21 mm case), the local indentation lead to multiple micro laminate
534 failure mechanisms. The observed failure mechanisms that have been classed under micro laminate
535 failure mechanisms were micro indentation, fibre tow splitting or loosening, micro matrix cracking and
536 localized fibre tow rupture within the weave.
537 The cumulative effect of all the micro damage mechanisms was observed using C-Scan while the detailed
538 observations were carried out using X-ray micro Tomography. Thus Figure 7 explains how the C-Scan
539 and tomography were used in support of each other to carry out multi-scale damage mechanism
540 observations. In this case, figure 7(a) shows C-scan of a 25 mm overlap width specimen, impacted at a
541 velocity of 6.7 ms^{-1} (4.5 J). This shows micro damage which was barely visible on visual inspection.
542 Figure 7(b) shows for the same specimen XMT view (xy-plane) of the inside of the specimen. This shows
543 fibre tow splitting and flattening due to micro indentation at interface zone of lamina 5 and 6 (counting
544 from impact side). Similarly in figure 7(c) for the same specimen xz-view along the plane cut by marked
545 line shown in figure 7(b) is presented. This shows fibre tow splitting and inter-laminar matrix cracks – the
546 dots in tows (out of plane) show extensive fibre tow splitting throughout thickness.
547 By comparing tomography scans of specimens at various impact velocities it was identified that in the
548 indentation zone the fabric started bending locally under the influence of impacting projectile. The matrix
549 allowed for the fibres to push on the underlying laminae. The bending of fibre weave and the shearing
550 against the matrix resulted in fibre tow splitting (loosening and consequently flattening). Depending on
551 the compactness of the lamina in the indentation zone (compactness in terms of resin, fibre and void
552 content.) and the impact velocity level the matrix directly under the impact load yielded locally and was
553 squeezed out from underneath the pressing fibres. Due to the weave however, such resin shear
554 deformation remained highly localized as the resin packed in the interstices locations. This made these
555 zones denser – and hence the cumulative effect of micro indentation and related damage mechanisms was
556 picked up in C-Scans and in transmission photography as a near circular disc or ring (this is also shown in

557 Figure 7a). For the cases where the extent of weave deformation was higher than the extent to which the
558 matrix could yield, local micro cracks at fibre resin interface and between plies developed.



559
560 **Figure 7:** A representative composite image obtained by combining a C-Scan and two XMT views of an
561 impacted specimen, showing micro-laminate failure mechanisms.

562 The results (summarized in Table 3), indicated that once the velocity was higher than a minimum
563 threshold in each case micro indentation phenomenon was observed. The minimum threshold varied with
564 the overlap width. If the velocity was lower than the minimum threshold then there was only perfectly
565 elastic response. The 21 mm overlap joint had lesser effective strength as compared to the 46 mm overlap
566 width joint due to smaller overlap area. Thus for the smaller overlap width case, the joint delaminated
567 without significant local indentation and at lower peak impact force. It will be shown with the aid of
568 simulation results later that as the projectile rebounded, for the smaller overlap width joint, the overall
569 bending of the joint rather than indentation became more pronounced and the effect of peel and
570 compressive stresses at the opposite joint free edges became apparent.

571 **(b) Macro Laminate failure mechanisms**

572 For those specimens that had sufficient overlap area to prevent disbonding followed by micro indentation,
573 the macro laminate failure mechanisms were observed. The details are as follows:

- 574 a. Macro indentation and bulging: For higher velocity cases, the observed macro indentation and bulging
575 was an amplified form of micro indentation phenomenon due to the increase in absorbed energy in the
576 absence of delamination. The underlying mechanisms, i.e. 'matrix yielding', 'fibre tow splitting',
577 'matrix cracking' and 'fibre push out' were the same as in micro indentation, however, it was the
578 scale that was magnified.
- 579 b. Matrix cracking: In-plane and out of plane matrix cracks developed in the indentation zone. These
580 generally resulted in complete loss of support to fibres.
- 581 c. Fibre push out: The fibres in the indentation zone were pushed out of the matrix. Further increase of
582 impact velocity lead to catastrophic failure/rupture of fibre tows in many cases.

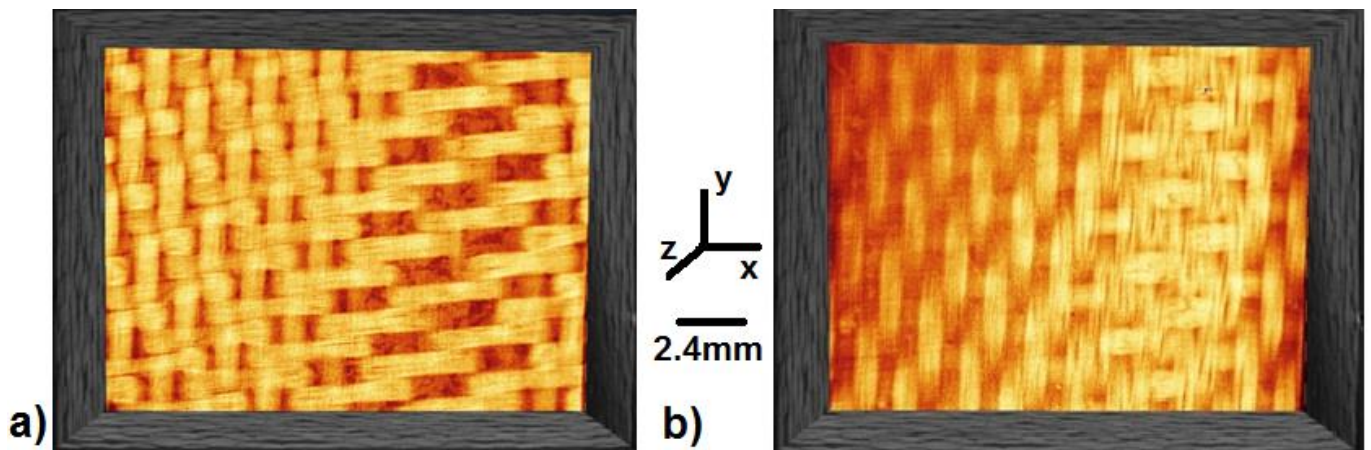
583 **Table 3: Relative severity of damage mechanisms for changing velocity and overlap-width**

		Case 1	Case 2	Case 3	Case 4	Case 5
	Damage mechanism	1.64J / 4.0ms ⁻¹	3.01J / 5.5ms ⁻¹	4.5J / 6.7ms ⁻¹	6.2J / 7.9ms ⁻¹	8.01J / 9.6ms ⁻¹
21 mm	Surface VID ¹	None	None	Barely visible (BV)	BV (< case 3)	BV (< case 4)
	Micro laminate ²	Some	Dominant	Dominant	Significant	Significant
	Macro laminate ³	None	None	Some	None	None
	Inter laminar ⁴	None	Joint Free edge	Dominant	Dominant	Dominant
25 mm	Surface VID ¹	None	None	BV	BV	Clearly visible (CV)
	Micro laminate ²	Some	Dominant	Dominant	-	-
	Macro laminate ³	None	None	Some	Dominant	Dominant
	Inter laminar ⁴	None	Joint Free edge	Joint Free edge	Dominant	Dominant
36 mm	Surface VID ¹	None	BV	BV (> case 2)	CV	Severe
	Micro laminate ²	None	Dominant	Dominant	-	-
	Macro laminate ³	None	None	Some	Dominant	Dominant
	Inter laminar ⁴	None	None	None	Some	Some

46 mm	Surface VID ¹	None	BV	BV (> case 2)	CV	Severe
	Micro laminate ²	None	Dominant	Dominant	-	-
	Macro laminate ³	None	None	Some	Dominant	Dominant
	Inter laminar ⁴	None	None	None	Some	Some
¹ visible impact damage at surface : ² as defined in section 3.2.1(a) : ³ as defined in section 3.2.1(b) : ⁴ as defined in section 3.2.2						

584

585 Figure 8 shows two sections of the lower surface of ply 1 (lamina 1), i.e. the back face lamina of a 25 mm
 586 overlap specimen. This was impacted at 9.6 ms⁻¹ velocity and suffered a combination of macro laminate
 587 failure mechanisms and inter-laminar failure (delamination/disbond). In this figure, only macro failure
 588 mechanisms have been discussed. In the first view in figure 8, the effect of matrix plastic deformation that
 589 led to fibre push out has been shown. In the second view (figure 8), extensive fibre tow splitting can be
 590 seen.



591

592 **Figure 8:** (a) Tomography slice ply 1 (i.e. bottom most ply) – note how the weave has been spaced out
 593 due to impact – This damage mechanism is being called fibre push out (b) Tomography slice ply 1 at
 594 bulge location – see the extensive two splitting in pushed out fibres

595 **3.2.2 Inter-laminar Failure Mechanisms - Delamination and Disbond**

596 Delamination for the purpose of XMT observations was defined as an inter-laminar matrix crack that
 597 extended continuously over a significant area and caused a separation between interfaces that was greater
 598 than 0.1 mm. Such a definition was necessary to distinguish between inter-laminar micro cracks in matrix
 599 from delamination. A disbond was defined as a delamination that took place at the joint interface (i.e.

This is an author's version of post print (final draft after referring) of the journal article in International Journal of Impact Engineering, Volume 80, June 2015, Pages 76-93, <https://doi.org/10.1016/j.ijimpeng.2015.02.003>
600 between the top and bottom adherends in the overlap region). A strong influence of overlap width on
601 delamination / disbond was observed. For co-cured, centrally impacted, single lap joints, this study found
602 that the maximum delamination damage occurred at joint interface and varying degree of delamination
603 damage occurred at other interfaces. The delamination damage was classified based on initiation and
604 propagation mechanism and the location (joint interface or adherend interfaces) at which it took place.
605 Thus a disbond took place through two mechanisms either independently of each other or in combination,
606 depending on the joint width.

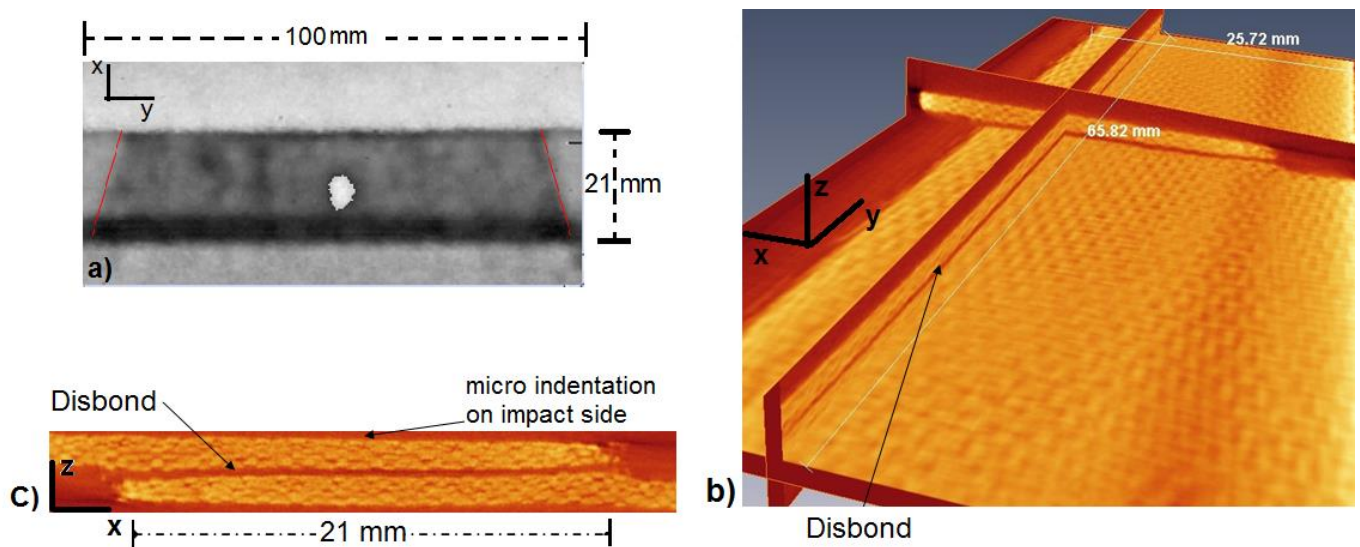
- 607 a. It propagated outwards from the region directly under the impactor in indentation zone. These
608 cracks generally stopped propagating or deflected when the collapsing weave from adjacent layers
609 blocked their path. Based on XMT and micrographs, it appeared that the mechanisms occurred
610 under mixed mode with type II component being more significant. The mechanism was more
611 pronounced for joints with greater overlap width.
- 612 b. Delamination/disbond initiating from back side joint free edge and propagating across the
613 interface without deflection. This is mainly due to type I loading and was more commonly
614 observed for narrower overlap joints.

615 Delamination at ply interfaces other than the bond interface was observed to take place through the first
616 of these two mechanisms with the exception of a case where the impactor had hit the joint nearer to the
617 constrained edges. In that case multiple delamination fronts starting from joint free edge were observed.
618 It was observed that whenever impactor velocity was 6.7 ms^{-1} (4.5 J impact energy) or greater, the
619 dominant failure mechanism for the 21 mm overlap width joints was disbonding. In case of 25 mm
620 overlap width joints, delamination was first observed when the impactor velocity was 7.9 ms^{-1} (6.2 J
621 impact energy). It was not the dominant mechanism, however, and occurred only when the applied
622 loading was off centre. When the impactor velocity was further increased to 9.6 ms^{-1} (8 J impact energy)
623 or higher, delamination became the dominant damage mechanism for this overlap width. In case of 36
624 and 46 mm overlap specimens no disbond and delamination was observed beyond the indentation zone

625 for impactor velocity of less than 9.6 ms^{-1} (impact energy less than 8 J. In these cases, the delamination
626 strongly interacted with other failure mechanisms.

627 In general, for woven composites the value of mode II fracture energy is about two to three times higher
628 than the mode I fracture energy [80, 81]. For the specimens in this study the experimental value of mode I
629 toughness G_{Ic} was 425 Jm^{-2} and mode II toughness G_{IIc} was 905 Jm^{-2} . Thus, type II delamination failure
630 was only observed when the loading conditions excluded significant mode I presence. In the current
631 problem the smaller the overlap region the greater will be the effect of peel stresses at the backside free-
632 edge of the joint and hence mode I type failure will dictate. This was especially true for the smallest
633 overlap (the 21 mm) case. In these joints no macro laminate failure mechanisms was observed. Even for
634 impactor velocity as high as 9.6 ms^{-1} (i.e. impact energy 8 J) very little surface and laminate damage and
635 almost total disbond failure was observed.

636 As an example the C-scan in figure 9a shows a 21 mm overlap width specimen (velocity 7.9 ms^{-1} or
637 impact energy 6.2 J) with central micro damage zone and the trapezoidal delamination zone. Using
638 tomography (for example figure 9b) the major delamination was verified to be present at joint interface
639 (lamina 4-5 interface). Similarly the micro indentation zone could also be identified.

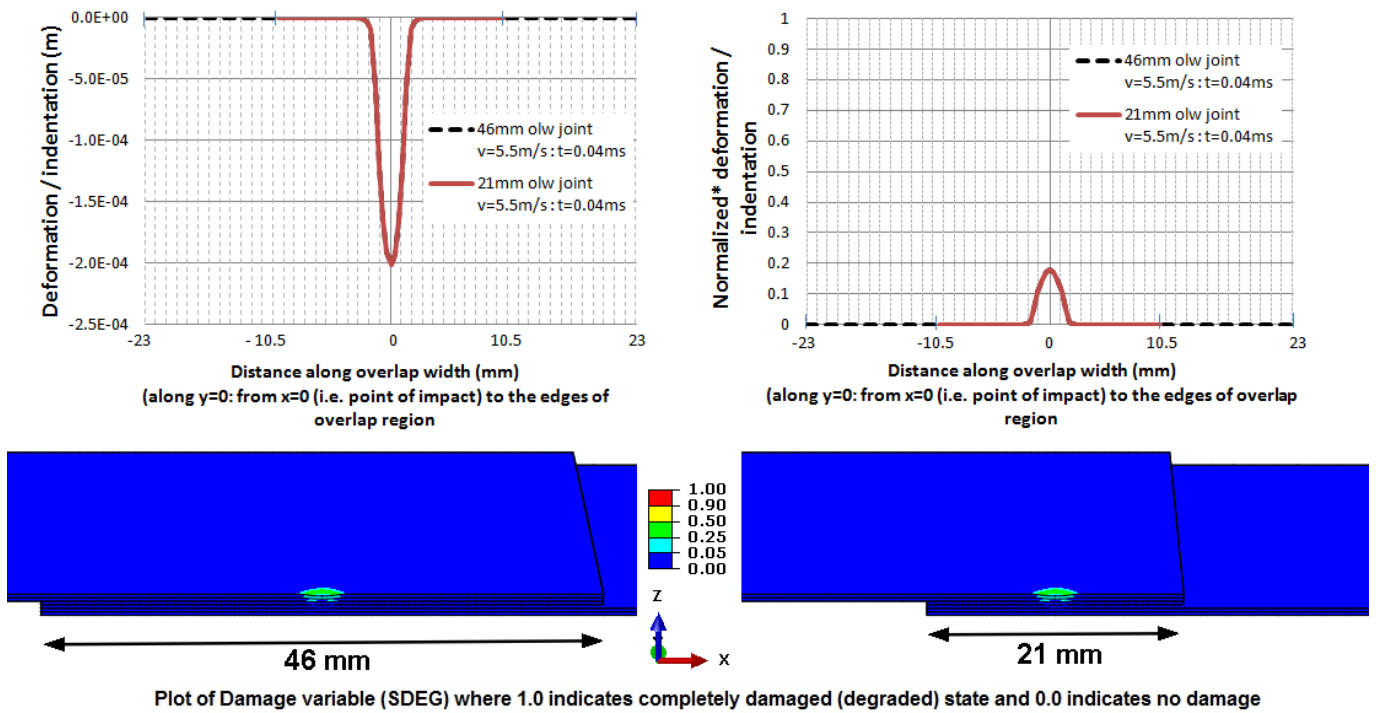


640
641 **Figure 9:** (a) C-scan showing a 21 mm overlap width specimen – (impactor velocity 7.9 ms^{-1}) – note the
642 central micro damage zone and the trapezoidal delamination (lines added at end of trapezoid for making
643 the shape prominent) (b) (c) Tomographic views of the same specimen showing failure at joint interface
644 (disbond)and micro indentation.

645 **3.3 Further explanation of damage based on FE simulation**

646 The damage area predicted by FE simulations has already been shown and discussed using figure 6. In
647 this section the deformed shapes and corresponding damage states for 21 and 46 mm joints have been
648 compared to explain the observed dependence of damage on overlap width. Figure 10 to 14 plots the
649 deformation and damage in lap joints of 21 mm and 46 mm overlap width for impact velocity of 5.5ms^{-1}
650 at different instances of time. In these figures in the first plot in each case the actual value of deformation
651 in meters is plotted against the x-distance along the overlap width for each case. Here $x = 0$ represents the
652 point of first impact/contact and positive distance is measured from $x = 0$ to impact-side free edge of the
653 lap joint, while negative distance is measured from $x=0$ to backside free edge of the joint. **The second**
654 **graph in each case shows the same deformation values plotted on a normalized scale. The normalization**
655 **is with respect to maximum out of plane deformation calculated for this impact velocity.**

656 Figure 10 shows the deformation and damage state at $t=0.04$ ms after the first contact (i.e. $t=0$). At this
657 stage the joint had just started to experience indentation damage below the tip of impactor. As shown at
658 this stage, none of the interfaces was completely degraded and the deformation could be considered
659 entirely elastic. **As expected, the deformed shapes for both overlaps at this stage were almost identical**
660 **and based on the normalized plot it can be seen that at this instance the out of plane deformation was**
661 **around 20% of its peak value.**

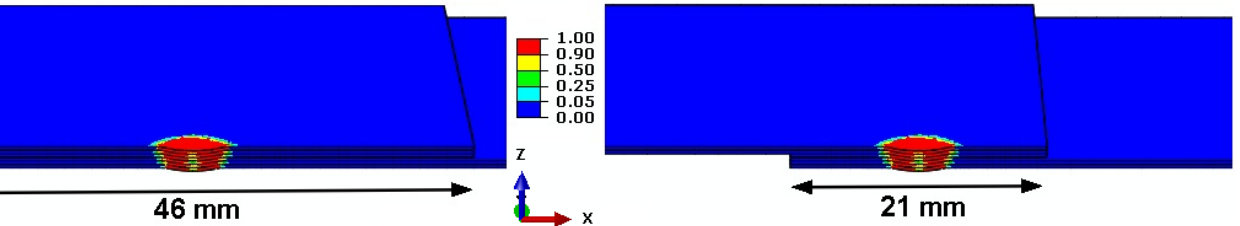
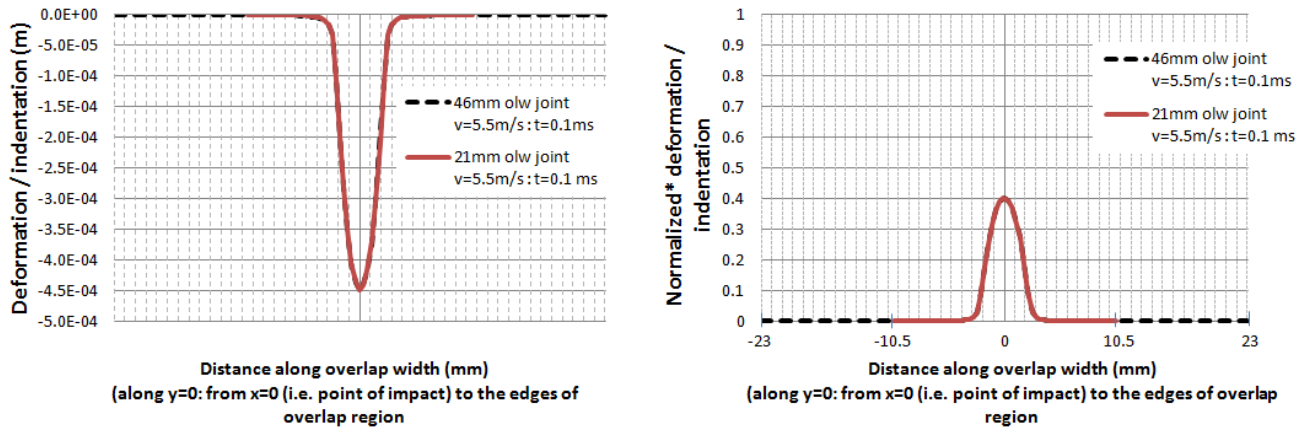


662

663 **Figure 10:** FE based deformation and damage plots for lap joints of 21 mm and 46 mm overlap width for
 664 impact velocity of 5.5ms^{-1} at 0.04 ms after initial contact.

665 Figure 11 presents the deformation and damage state at $t = 0.1$ ms. Till this stage the projectile had moved
 666 further down and the indentation at this stage was around 40% of the peak indentation experienced by the
 667 joints for this velocity (shown in the second plot in Figure 11). By this stage all interfaces had
 668 experienced indentation failure just below the point of impact. It is interesting to note that the shape of
 669 damaged zone below the first interface is in the form of a near circular ring and this was in keeping with
 670 the experimentally observed shape of damage zone for low velocity impacts.

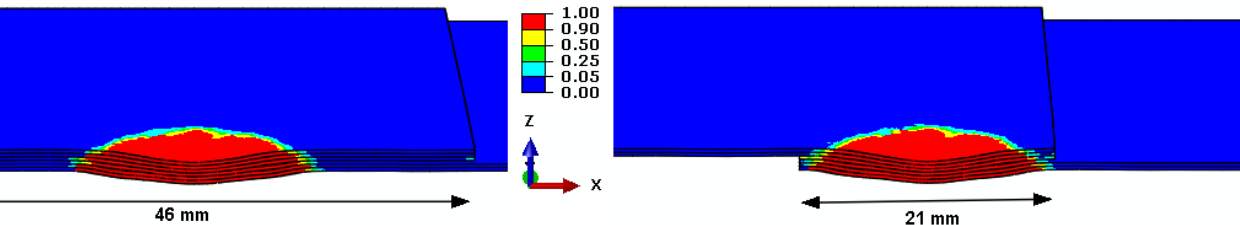
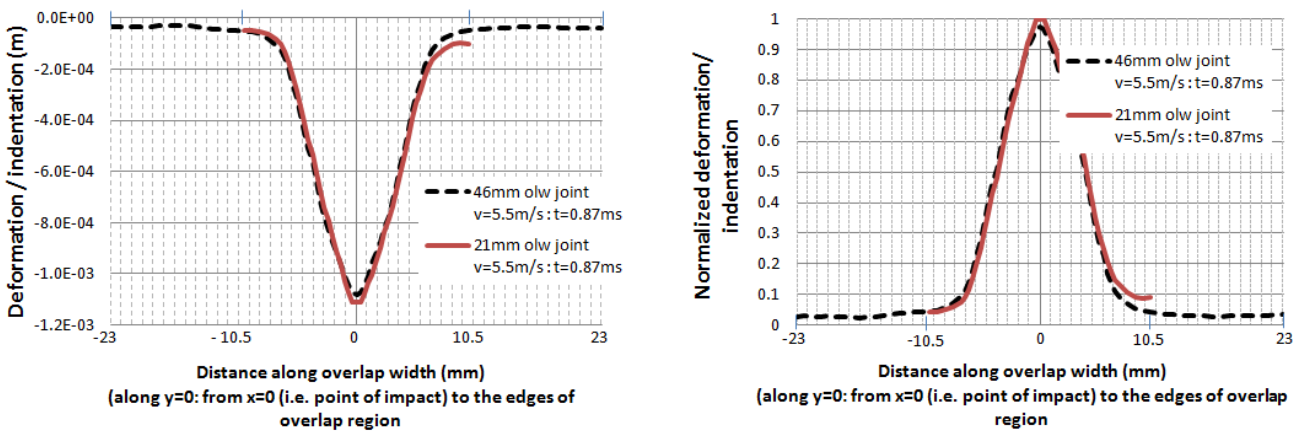
671 As the projectile moved further down the peak deformation for this impact velocity was experienced at
 672 $t=0.87\text{ms}$ after the initial contact. This has been shown in figure 12. **It is interesting to note that for the**
 673 **21mm joint the impact side joint free edge has slightly greater downward deformation than the backside**
 674 **joint free edge. This indicates that the peel separation of joint is more likely from the back side joint free**
 675 **edge and the impact side joint free edge is acting almost as a virtual hinge (pivot) point for the opening at**
 676 **the opposite free edge. A closer look revealed that by this stage for 21 mm joint a delamination/bond**
 677 **failure initiating from the backside joint free edge had appeared and this was in addition to the damage of**
 678 **interface that had expanded outwards from below the indentation zone.**



Plot of Damage variable (SDEG) where 1.0 indicates completely damaged (degraded) state and 0.0 indicates no damage

679

680 **Figure 11:** FE based deformation and damage plots for lap joints of 21 mm and 46 mm overlap width for
681 impact velocity of 5.5ms^{-1} at 0.1 ms after initial contact

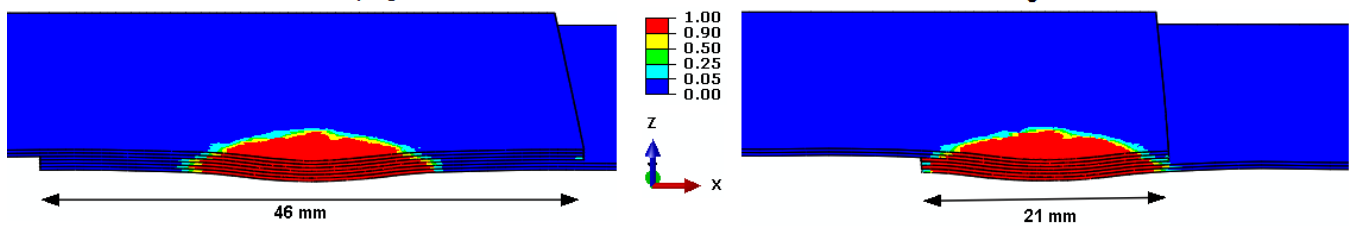
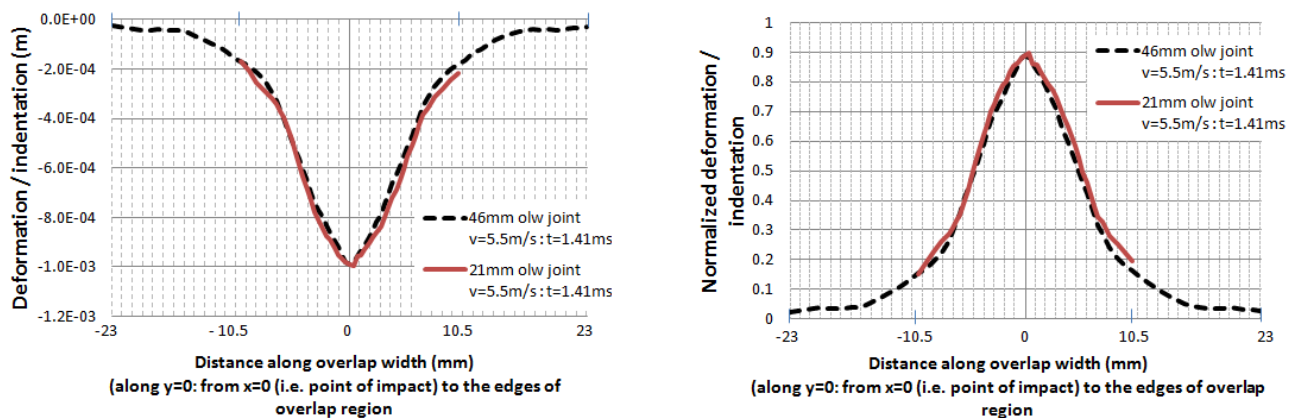


Plot of Damage variable (SDEG) where 1.0 indicates completely damaged (degraded) state and 0.0 indicates no damage

682

683 **Figure 12:** FE based deformation and damage plots for lap joints of 21 mm and 46 mm overlap width for
684 impact velocity of 5.5ms^{-1} at 0.87 ms after initial contact.

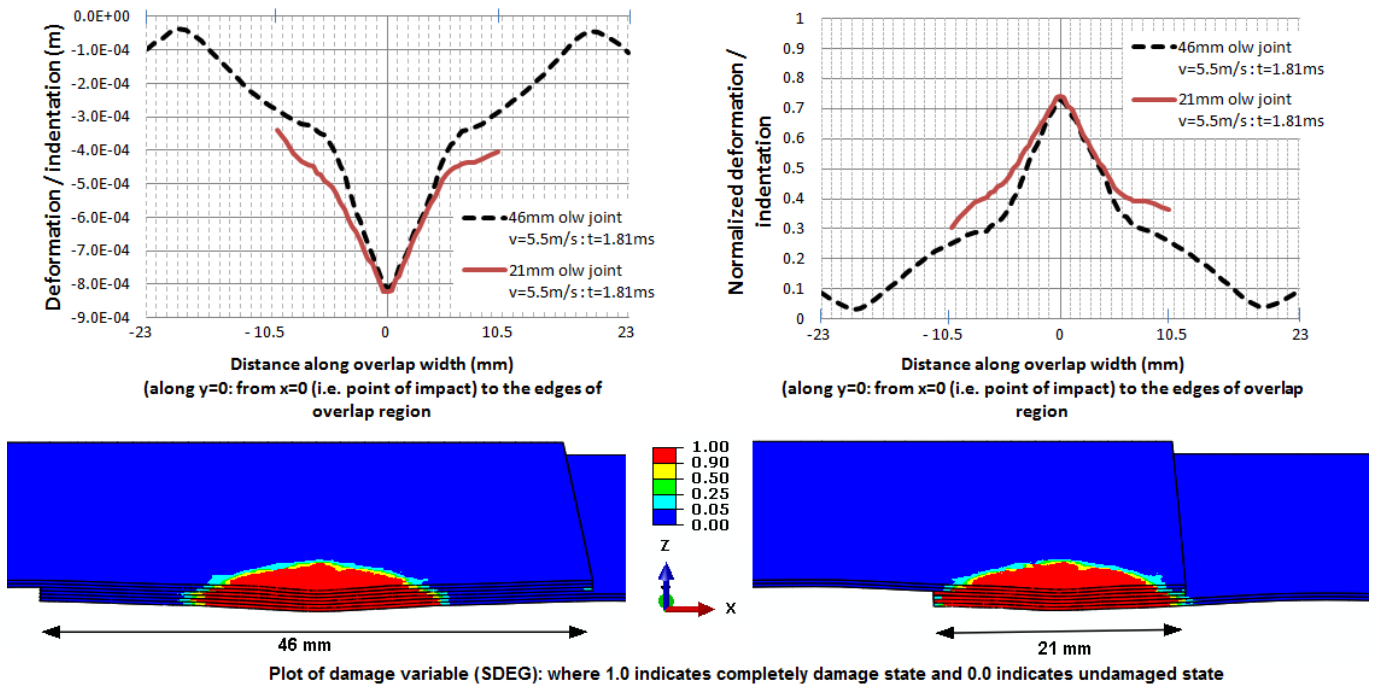
685 The difference in bending shape became much more pronounced after this stage, as the projectile
686 rebounded. This has been shown with the help of figure 13 and 14 which correspond to $t=1.41\text{ms}$ and
687 1.81ms respectively. For the 21 mm joint, the joint edges had undergone considerable deformation and
688 thus delamination that initiated from these edges could propagate towards the point of initial impact. On
689 the other hand for the 46 mm joint, the only delamination front that propagated was from the impact
690 location towards joint free edges. This resulted in significantly greater percentage delamination with
691 respect to overlap width for 21 mm joint. Since the simulation did not cater for macro laminate failure
692 mechanisms, the delamination that started from either of these points propagated purely on the basis of
693 mode-mix of fracture for the cohesive zone. In reality, as explained earlier, for larger joints the macro
694 laminate failure mechanisms limited the extent of damage area. In such cases the damage may be limited
695 to a smaller area but it is more severe in terms of mechanisms involved (e.g. local weave failure). It can
696 be seen from figure 14 that during the rebound phase, once the stress wave had reflected, the return path
697 for deformation profile was not the same in both cases because of the greater degradation of overlap
698 region for the 21mm joint. In order to sum up the discussion figure 15 shows the damage at each interface
699 of both the joints at the same instance as discussed in figure 14.

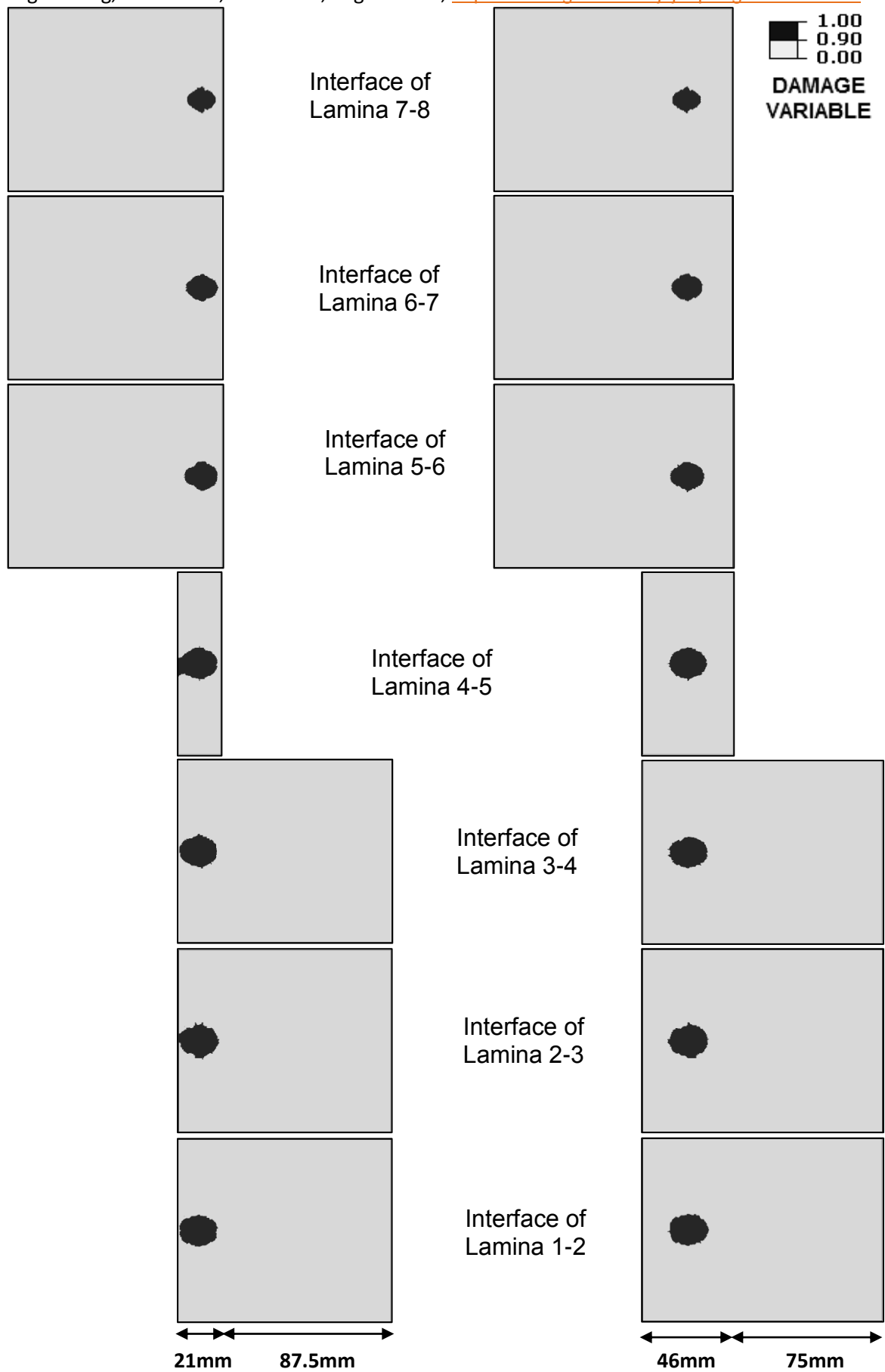


Plot of Damage variable (SDEG) where 1.0 indicates completely damaged (degraded) state and 0.0 indicates no damage

700

701 **Figure 13:** FE based deformation and damage plots for lap joints of 21 mm and 46 mm overlap width for
 702 impact velocity of 5.5ms^{-1} at 1.41 ms after initial contact.





708 **Figure 15: FE based damage area plots for all interfaces of lap joints of 21 mm and 46 mm overlap**
709 ***width for impact velocity of 5.5ms^{-1} at 1.81ms after initial contact***

710 **3.4 Generalization of results and the concept of characteristic overlap width**

711 Grouping the results discussed in previous section in terms of change in dominant damage mechanism
712 with increasing impact velocity for a given overlap width, highlights three discerning patterns. These are;

713 **Pattern 1:** In pattern 1, for velocities up to 5.5ms^{-1} , '*Micro damage mechanisms*' were dominant whereas
714 if the impact velocity lied between 5.5ms^{-1} to 6.7ms^{-1} then '*Localized indentation related delamination*
715 *in impact zone*' became dominant. On increasing the impact velocity further (i.e. 6.7ms^{-1} to 9.6ms^{-1}),
716 '*Delamination at joint interface (disbonding)*' became the dominant failure mechanism.

717 **Pattern 2:** In pattern 2, for velocities up to 6.7ms^{-1} , the damage pattern was similar to Pattern 1, whereas
718 if the impact velocity was increased further (i.e. 6.7ms^{-1} to 9.6ms^{-1}) then '*Macro Laminate failure*
719 *mechanisms*' became dominant at velocities higher than 6.7ms^{-1} (i.e. no significant global delamination
720 and disbonding took place)

721 **Pattern 3:** In pattern 3, again for velocities up to 6.7ms^{-1} , the damage pattern was similar to Pattern 1 and
722 2, whereas, if the impact velocity was increased further (i.e. 6.7ms^{-1} to 9.6ms^{-1}) then instead of one
723 dominant damage mechanism a balanced mix of '*Disbond and Macro laminate failure mechanisms*' was
724 observed.

725 In summary, these patterns were observed as follows:

- 726 a. Pattern 1 was mainly observed for 21 mm overlap joint
- 727 b. Pattern 2 was observed for 36 and 46 mm overlap width joint.
- 728 c. Pattern 3 was observed for the 25 mm overlap width joint.

729 Thus these observations pointed to the fact that in the low velocity/energy regime (the one observed in
730 this study) there appeared to exist a lower characteristic overlap width such that if the overlap width was
731 less than the characteristic width the dominant damage mechanism was always a combination of micro

This is an author's version of post print (final draft after referring) of the journal article in International Journal of Impact Engineering, Volume 80, June 2015, Pages 76-93, <https://doi.org/10.1016/j.ijimpeng.2015.02.003>
732 damage under the impactor nose and a delamination/disbond that initiated from back side joint free edge
733 and propagated across the joint interface, primarily due to bending, resulting in peel type loading of joint
734 (pattern 1). Similarly for the same energy and velocity range, an upper characteristic width could also be
735 defined such that if the overlap width was greater than this upper characteristic width; the dominant
736 failure was always a combination of micro and macro laminate damage mechanisms, with no or little
737 inter-laminar failure (i.e. pattern 2). Interfacial matrix cracks, however, existed in the indentation zone but
738 these did not appear to propagate in a continuous manner. For the energy and velocity range investigated
739 in this study, the lower characteristic width in this case was found to be around 21 mm while the upper
740 characteristic width was found to be around 35 mm. In between the two limits pattern 3 dominated. This
741 characteristic width is specific to a particular energy range, joint geometry and boundary conditions. In
742 future work, it may be possible to show the relationship of this width with the impactor **tip diameter, tip**
743 **shape and material**.

744 **4. Conclusions**

745 The paper has given a detailed account of impact induced damage mechanisms observed for composite
746 lap joint having different overlap widths (areas), which were impacted with increasing velocities. The
747 damage mechanism observations were carried out at various length scales using mainly a combination of
748 x-ray micro-tomography and ultrasonic C-scan. The damage mechanism observations were supplemented
749 with detailed delamination modelling (FE analysis) to aid the understanding of how the damage
750 mechanisms changed for different widths in response to increasing velocities.

751 Based on these observations and understanding from FE analysis it has been suggested that the dominant
752 damage mechanism for a given velocity range is a function of overlap width. Thus, if the overlap width is
753 less than the lower characteristic width, then disbonding dominates as a failure mechanism, for velocities
754 that can cause visible impact damage. Whereas, if the overlap width is greater than the upper
755 characteristic width then macro laminate failure mechanisms rather than delamination and disbonding
756 dominates for comparable velocities as in previous case. If the overlap width is between these two limits
757 then a balanced mix of delamination/disbonding and laminate failure mechanisms take place.

This is an author's version of post print (final draft after referring) of the journal article in International Journal of Impact Engineering, Volume 80, June 2015, Pages 76-93, <https://doi.org/10.1016/j.ijimpeng.2015.02.003>
758 Further work is required to explore if this parameter can be used as a design guide for such joints based
759 on residual strength of such impacted joints. It is also acknowledged that the choice of boundary
760 condition (in particular the free breadth of joint) and the choice of impactor shape and material (e.g. if the
761 impactor is of a material that is softer than the joint material) may change the observed damage pattern.

762 **Acknowledgements:** The corresponding author gratefully acknowledges the financial support of NUST,
763 Pakistan and The University of Manchester, UK for this work. He also wishes to thank Dr. David Bond
764 who proposed this research topic and introduced the first author to this fascinating area. Gratitude is due
765 to Professor Paul Hogg who has always provided me with material and moral support during this work
766 and beyond it. In addition support of Dr. Q. M. Li for the use of his impact gun and Professor P. Withers
767 for the use of x-ray micro tomography facilities is highly acknowledged. The author is also indebted to
768 the two anonymous reviewers who through their detailed feedback and questions have contributed
769 tremendously to the improvement of this paper.

770 References

- 771 [1] I. Herszberg, F. Dharmawan, R.S. Thomson, H.C.H. Li, E. Gellert, Geometry and damage effects in a composite
772 marine T-joint, *Composite Structures*, 66: (2004) 181 - 187.
- 773 [2] I. Herszberg, H.C.H. Li, F. Dharmawan, A.P. Mouritz, M. Nguyen, J. Bayandor, Damage assessment and
774 monitoring of composite ship joints, *Composite Structures*, 67 (2005) 205 - 216.
- 775 [3] S. Li, M.D. Thouless, A.M. Waas, J.A. Schroeder, P.D. Zavattieri, Use of mode-I cohesive-zone models to
776 describe the fracture of an adhesively-bonded polymer-matrix composite, *Composites Science and Technology*,
777 65 (2005) 281–293.
- 778 [4] S. Li, M.D. Thouless, A.M. Waas, J.A. Schroeder, P.D. Zavattieri, Competing failure mechanisms in mixed-mode
779 fracture of an adhesively bonded polymer-matrix composite, *International Journal of Adhesion and Adhesives*, 26
780 (2006) 609-616.
- 781 [5] S. Li, M.D. Thouless, A.M. Waas, J.A. Schroeder, P.D. Zavattieri, Mixed-mode cohesive-zone models for fracture
782 of an adhesively bonded polymer-matrix composite, *Engineering Fracture Mechanics*, 73 (2006) 64-78.
- 783 [6] S. Gómez, J. Oñoro, J. Pecharromán, A simple mechanical model of a structural hybrid adhesive/riveted single
784 lap joint, *International Journal of Adhesion and Adhesives*, 27 (2007) 263-267.
- 785 [7] I.A. Ashcroft, S. Erpolat, J. Tyrer, Damage Assessment in Bonded Composite Joints, *Key Engineering Materials*,
786 245-246 (2003) 501-508.
- 787 [8] M.M.A. Wahab, I.A. Ashcroft, A.D. Crocombe, P.A. Smith, Fatigue crack propagation in adhesively bonded
788 joints, *Key Engineering Materials*, 251-252 (2003) 229-234.
- 789 [9] K.D. Potter, F.J. Guild, H.J. Harvey, M.R. Wisnom, R.D. Adams, Understanding and control of adhesive crack
790 propagation in bonded joints between carbon fibre composite adherends I. Experimental, *International Journal of*
791 *Adhesion and Adhesives*, 21 (2001) 435-443.
- 792 [10] M.O.W. Richardson, M.J. Wisheart, Review of low-velocity impact properties of composite materials,
793 *Composites Part A: Applied Science and Manufacturing*, 27 (1996) 1123-1131.
- 794 [11] G.A. Bibo, P.J. Hogg, The role of reinforcement architecture on impact damage mechanisms and post-impact
795 compression behaviour, *Journal of Materials Science*, 31 (1996) 1115-1137.
- 796 [12] S. Abrate, *Impact on Composite Structures*, Cambridge University Press, Cambridge, 1998.

This is an author's version of post print (final draft after referring) of the journal article in International Journal of Impact Engineering, Volume 80, June 2015, Pages 76-93, <https://doi.org/10.1016/j.ijimpeng.2015.02.003>

- 797 [13] C. Soutis, P.T. Curtis, Prediction of the post-impact compressive strength of CFRP laminated composites,
798 Composites Science and Technology, 56 (1996) 677-684.
- 799 [14] P. Robinson, G.A.O. Davies, Impactor mass and specimen geometry effects in low velocity impact of
800 laminated composites, International Journal of Impact Engineering, 12 (1992) 189-207.
- 801 [15] G. Davies, P. Robinson, Predicting failure by debonding/delamination, AGARD, Debonding/Delamination of
802 Composites 28 p(SEE N 93-21507 07-24), (1992).
- 803 [16] R.Olsson, Mass criterion for wave controlled impact response of composite plates, Composites Part A:
804 Applied Science and Manufacturing, 31 (August 2000) 879-887.
- 805 [17] M.P.F. Sutcliffe, C. Monroy Aceves, W.J. Stronge, R.S. Choudhry, A.E. Scott, Moderate speed impact damage
806 to 2D-braided glass-carbon composites, Composite Structures, 94 (2012) 1781-1792.
- 807 [18] Z. Zhang, M. Richardson, Low velocity impact induced damage evaluation and its effect on the residual
808 flexural properties of pultruded GRP composites, Composite Structures, 81 (2007) 195-201.
- 809 [19] P.J. Schilling, B.R. Karedla, A.K. Tatiparthi, M.A. Verges, P.D. Herrington, X-ray computed microtomography of
810 internal damage in fiber reinforced polymer matrix composites, Composites Science and Technology, 65 (2005)
811 2071-2078.
- 812 [20] H. Ullah, A.R. Harland, V.V. Silberschmidt, Evolution and interaction of damage modes in fabric-reinforced
813 composites under dynamic flexural loading, Composites Science and Technology, 92 (2014) 55-63.
- 814 [21] R.S. Choudhry, R. Day, S. Li, Characterization of impact induced damage modes in composites using X-ray
815 microtomography, in: 17th International Conference on Composite Materials, ICCM 17, Edinburgh, UK, 2009.
- 816 [22] P. Potluri, T. Sharif, D. Jetavat, A. Aktas, R.S. Choudhry, P. Hogg, Bench marking of 3D performing strategies,
817 in: 17th International Conference on Composite Materials, ICCM 17, Edinburgh, UK, 2009.
- 818 [23] D. Feng, F. Aymerich, Finite element modelling of damage induced by low-velocity impact on composite
819 laminates, Composite Structures, 108 (2014) 161-171.
- 820 [24] S. Abrate, Modeling of impacts on composite structures, Composite structures, 51 (2001) 129-138.
- 821 [25] Z. Zou, S.R. Reid, S. Li, A continuum damage model for delaminations in laminated composites, Journal of the
822 Mechanics and Physics of Solids, 51 (2003) 333-356.
- 823 [26] S. Li, S.R. Reid, Z. Zou, Modelling damage of multiple delaminations and transverse matrix cracking in
824 laminated composites due to low velocity lateral impact, Composites Science and Technology, 66 (2006) 827-836.
- 825 [27] R.S. Choudhry, R. Day, S. Li, Modelling failure and damage growth in lap joints of woven GFRP composites – A
826 comparison of failure modes, in: DFC-10, 10th Deformation and Fracture of Composites Conference, Krot
827 Research Institute, Sheffield, UK, 2009.
- 828 [28] E.J. Barbero, Finite element analysis of composite materials, CRC press, 2007.
- 829 [29] E.J. Barbero, Finite Element Analysis of Composite Materials using Abaqus™, CRC Press, 2013.
- 830 [30] E. Barbero, F. Cosso, R. Roman, T. Weadon, Determination of material parameters for Abaqus progressive
831 damage analysis of E-Glass Epoxy laminates, Composites Part B: Engineering, 46 (2013) 211-220.
- 832 [31] O. Allix, P. Ladeveze, A. Corigliano, Damage analysis of interlaminar fracture specimens, Composite Structures,
833 31 (1995) 61-74.
- 834 [32] T. Tay, G. Liu, V. Tan, X. Sun, D. Pham, Progressive failure analysis of composites, Journal of Composite
835 Materials, (2008).
- 836 [33] S.-H. Lim, S. Li, Energy release rates for transverse cracking and delaminations induced by transverse cracks in
837 laminated composites, Composites Part A: Applied Science and Manufacturing, 36 (2005) 1467-1476.
- 838 [34] H. Chai, Three-dimensional fracture analysis of thin-film debonding, International Journal of Fracture, 46
839 (1990) 237-256.
- 840 [35] W.-L. Yin, J. Wang, The energy-release rate in the growth of a one-dimensional delamination, Journal of
841 Applied Mechanics, 51 (1984) 939-941.
- 842 [36] M. Wisheart, M. Richardson, The finite element analysis of impact induced delamination in composite
843 materials using a novel interface element, Composites part A: Applied science and manufacturing, 29 (1998) 301-
844 313.
- 845 [37] G. Alfano, M. Crisfield, Finite element interface models for the delamination analysis of laminated composites:
846 mechanical and computational issues, International journal for numerical methods in engineering, 50 (2001)
847 1701-1736.
- 848 [38] X.-P. Xu, A. Needleman, Numerical simulations of fast crack growth in brittle solids, Journal of the Mechanics
849 and Physics of Solids, 42 (1994) 1397-1434.

This is an author's version of post print (final draft after referring) of the journal article in International Journal of Impact Engineering, Volume 80, June 2015, Pages 76-93, <https://doi.org/10.1016/j.ijimpeng.2015.02.003>

- 850 [39] M. Nishikawa, T. Okabe, N. Takeda, Numerical simulation of interlaminar damage propagation in CFRP cross-
851 ply laminates under transverse loading, International Journal of Solids and Structures, 44 (2007) 3101-3113.
- 852 [40] L. Iannucci, progressive failure modelling of woven carbon composites under impact, International Journal of
853 Impact Engineering 32 (2006) 1013-1043.
- 854 [41] M. Donadon, L. Iannucci, B. Falzon, J. Hodgkinson, S. De Almeida, A progressive failure model for composite
855 laminates subjected to low velocity impact damage, Computers & Structures, 86 (2008) 1232-1252.
- 856 [42] D.J. Elder, R.S. Thomson, M.Q. Nguyen, M.L. Scott, Review of delamination predictive methods for low speed
857 impact of composite laminates, Composite Structures, 66 (2004) 677-683.
- 858 [43] H. Ullah, A.R. Harland, V.V. Silberschmidt, Damage and fracture in carbon fabric reinforced composites under
859 impact bending, Composite Structures, 101 (2013) 144-156.
- 860 [44] A. Puck, H. Schürmann, Failure analysis of FRP laminates by means of physically based phenomenological
861 models, Composites Science and Technology, 62 (2002) 1633-1662.
- 862 [45] C.G. Davila, P.P. Camanho, Failure criteria for FRP laminates in plane stress, in: NASA TM 212663, NASA -
863 Langley Research Centre, 2003, pp. 1-23.
- 864 [46] S.W. Tsai, Section 8, Failure Criteria, Think Composites, Palo, Alto, 1992.
- 865 [47] Z. Hashin, Failure criteria for unidirectional fiber composites, Journal of applied mechanics, 47 (1980) 329-334.
- 866 [48] J. Oliver, A consistent characteristic length for smeared cracking models, International Journal for Numerical
867 Methods in Engineering, 28 (1989) 461-474.
- 868 [49] P.P. Camanho, C.G. Davila, S.T. Pinho, Fracture analysis of composite co-cured structural joints using
869 decohesion elements, Fatigue and Fracture of Engineering Materials and Structures, 27 (2004) 745-757.
- 870 [50] Y. Shi, T. Swait, C. Soutis, Modelling damage evolution in composite laminates subjected to low velocity
871 impact, Composite Structures, 94 (2012) 2902-2913.
- 872 [51] E.-H. Kim, M.-S. Rim, I. Lee, T.-K. Hwang, Composite damage model based on continuum damage mechanics
873 and low velocity impact analysis of composite plates, Composite Structures, 95 (2013) 123-134.
- 874 [52] H. Kim, K.T. Kedward, S.L. Steber, Mechanisms of damage formation in transversely impacted glass/epoxy
875 bonded lap joints, Journal of Composite Materials, 39 (2005) 2039 - 2052.
- 876 [53] V.V. Bhamare, Transverse Impact Characteristics of adhesively bonded composite single lap joint, in: College
877 of Engineering, Wichita State University, 2006.
- 878 [54] M. Quaresimin, M. Ricotta, Life prediction of bonded joints in composite materials, The Third International
879 Conference on Fatigue of Composites, 28 (2006) 1166-1176.
- 880 [55] M. Quaresimin, M. Ricotta, Stress intensity factors and strain energy release rates in single lap bonded joints
881 in composite materials, Composites Science and Technology, 66 (2006) 647-656.
- 882 [56] R.A. Odi, C.M. Friend, An improved 2D model for bonded composite joints, International Journal of Adhesion
883 and Adhesives, 24 (2004) 389-405.
- 884 [57] K.-S. Kim, Y.-M. Yi, G.-R. Cho, C.-G. Kim, Failure prediction and strength improvement of uni-directional
885 composite single lap bonded joints, Composite Structures, 82 (2008) 513-520.
- 886 [58] P.J. Hogg, G.A. Bibo, Impact and damage tolerance, in: J.M. Hodgkinson (Ed.) Mechanical testing of
887 advanced fibre composites, Woodhead Publishing Ltd, Cambridge, England, 2000, pp. 211-244.
- 888 [59] A.S. Kaddour, WWFE II Damage exercise benchmark test cases, in: International Conference on Composite
889 Materials 16 (ICCM16), Kyoto, Japan, 2007.
- 890 [60] P.D. Soden, A.S. Kaddour, M.J. Hinton, Recommendations for designers and researchers resulting from the
891 world-wide failure exercise, Composites Science and Technology, 64 (2004) 589-604.
- 892 [61] P.P. Camanho, C.G. Davila, Mixed-mode decohesion finite elements for the simulation of delamination in
893 composite materials, in: NASA TM 211737, NASA, 2002, pp. 37.
- 894 [62] L.W. Davies, R.J. Day, D. Bond, A. Nesbitt, J. Ellis, E. Gardon, Effect of cure cycle heat transfer rates on the
895 physical and mechanical properties of an epoxy matrix composite, Composites Science and Technology, 67 (2007)
896 1892-1899.
- 897 [63] J.L. Abot, A. Yasmin, A.J. Jacobsen, I.M. Daniel, In-plane mechanical, thermal and viscoelastic properties of a
898 satin fabric carbon/epoxy composite, Composites Science and Technology, 64 (2004) 263-268.
- 899 [64] Tactile pressure indicating sensor film, in: www.sensorprod.com, Sensor Products Inc., Madison, NJ 07940
900 USA, 2008.
- 901 [65] R.S. Choudhry, Characterisation and modelling of impact damage in bonded joints of woven fibre polymeric
902 composites (PhD Thesis), in: The School of MACE, The University of Manchester, Manchester, 2009.
- 903 [66] A.C. Kak, M. Slaney, Principles of Computerized Tomographic Imaging, SIAM Publishers (IEEE Press), 1998.

This is an author's version of post print (final draft after referring) of the journal article in International Journal of Impact Engineering, Volume 80, June 2015, Pages 76-93, <https://doi.org/10.1016/j.ijimpeng.2015.02.003>

- 904 [67] Section 37.1.1, Mechanical contact properties: overview, in: Abaqus Analysis User's Guide (v6.13), ABAQUS,
905 Inc, 2013.
- 906 [68] Section 29.6.8, Continuum shell element library, in: Abaqus Analysis User's Guide (v6.13), ABAQUS, Inc, 2013.
- 907 [69] Section 32.5.9, Three-dimensional cohesive element library, in: Abaqus Analysis User's Guide (v6.13),
908 ABAQUS, Inc, 2013.
- 909 [70] Section 26.5, Cohesive elements, in: ABAQUS Analysis User's Manual (v6.6ef), ABAQUS, Inc., 2006.
- 910 [71] S. Li, S.R. Reid, P.D. Soden, M.J. Hinton, The Nonlinear Structural Response of Laminated Composites, in: 6th
911 Int. Conf. Deformation and Fracture of Composites (DFC-6), Manchester, UK, 2001.
- 912 [72] Section 26.6.8, Continuum shell element library, in: ABAQUS Analysis User's Manual (v6.10), ABAQUS, Inc,
913 2010.
- 914 [73] Section 3.6.8, Transverse shear stiffness in composite shells and offsets from the midsurface, in: ABAQUS
915 Theory Manual (v6.10), ABAQUS, Inc, 2010.
- 916 [74] S. Heimbs, S. Schmeer, P. Middendorf, M. Maier, Strain rate effects in phenolic composites and phenolic-
917 impregnated honeycomb structures, Composites Science and Technology, 67 (2007) 2827-2837.
- 918 [75] Section 1.2.17, VUMAT in: Abaqus User Subroutines Reference Manual (v6.10), ABAQUS, Inc, 2010.
- 919 [76] Section 26.5.6, Defining the constitutive response of cohesive elements using a traction-separation
920 description, in: ABAQUS Analysis User's Manual (v6.6ef), ABAQUS, Inc., 2006.
- 921 [77] E.J. Barbero, Chapter 10, Delamination, in: Finite Element Analysis of Composite Materials using Abaqus™,
922 CRC Press (Taylor and Francis Group), USA, 2013, pp. 353-375.
- 923 [78] M.L. Benzeggagh, M. Kenane, Measurement of mixed-mode delamination fracture toughness of
924 unidirectional Glass/Epoxy composites with mixed mode bending apparatus, Composites Science and Technology,
925 56 (1996) 439 - 449.
- 926 [79] Section 32.5.6, Interpretation of Material Properties, , in: ABAQUS analysis user manual (v6.10), ABAQUS, Inc,
927 2010.
- 928 [80] J.-K. Kim, M.-L. Sham, Impact and delamination failure of woven-fabric composites, Composites Science and
929 Technology, 60 (2000) 745-761.
- 930 [81] P. Robinson, J.M. Hodgkinson, Interlaminar fracture toughness, in: J.M. Hodgkinson (Ed.) Mechanical testing
931 of advanced fibre composites, Woodhead Publishing Ltd, Cambridge, England, 2000, pp. 170-207.

932